Earth, Planets and Space

FULL PAPER Open Access

Peak ground motions and characteristics of nonlinear site response during the 2018 Mw 6.6 Hokkaido eastern Iburi earthquake

Yadab P. Dhakal*, Takashi Kunugi, Takeshi Kimura, Wataru Suzuki and Shin Aoi

Abstract

The observed peak ground accelerations and peak ground velocities (PGVs) of the 2018 Mw 6.6 Hokkaido eastern Iburi earthquake generally followed the median values from ground motion prediction equations with reasonable errors at fault distances ≥ 50 km. However, at smaller distances, the equations significantly underestimated the peak ground motions, and it was eminent for PGVs. A comparison of surface-to-borehole spectral ratios of S-waves during the mainshock and other events revealed that the sites at smaller distances experienced various degrees of nonlinear site response. The two most widely known characteristics of nonlinear site response are the weakening of higher-frequency components and shifting of predominant frequencies to lower ones in comparison with the linear site response. At one of the sites that recorded the largest intensity of 7 in JMA scale of 0–7, the latter nonlinear effect was so dominant that the ground motions around the new predominant frequency got intensified by one order of magnitude in comparison with that during the weak-motions. Two sites, which were closely located, recorded vertical peak ground accelerations exceeding 1 g for the up-going motions. The recordings showed asymmetric waveforms and amplitudes characteristics of the nonlinear site response in extreme vertical ground motions recorded during a few earthquakes in the past. Few sites having lower vertical peak ground accelerations were also suspected of being experienced nonlinear site response on vertical motions. These findings suggest taking a cautious approach to enumerate the reduction in amplification at higher frequencies using the single-station horizontal-to-vertical (H-to-V) spectral ratio technique. However, we found that the H-to-V technique was still useful to detect nonlinearity. Finally, an ad hoc equation was derived to correct the nonlinear site amplification in predicting horizontal PGVs with respect to one of the most widely used attenuation models in Japan. The results indicated that the effect was much stronger for a larger input motion than that for a proportional change in the Vs30 values.

Keywords: Nonlinear site response, Degree of nonlinearity, Ground motion prediction equations, Spectral ratios, Peak ground acceleration, Peak ground velocity, The 2018 Hokkaido eastern Iburi earthquake

Introduction

The 2018, Mw 6.6 Hokkaido eastern Iburi earthquake occurred on September 6, 03:08 JST (UTC + 9 h). The Mw value of 6.6 was determined by F-net NIED (Okada et al. 2004). The Mw values determined by USGS (2018) and GCMT (e.g., Ekström et al. 2012) were 6.6 and 6.7, respectively. The Japan Meteorological Agency (JMA) magnitude (Mj) was 6.7, and the focal depth was 37 km. The epicenter of the earthquake was located on the western foreland area of a collision zone known as Hidaka collision zone (e.g., Kimura 1996). Earthquakes of comparable magnitudes with similar focal depths have repeatedly occurred in the region (e.g., Kita et al. 2014). The 2018 earthquake caused loss of 42 lives, resulted into total collapse of 462 and partial collapse of 1570 residential buildings, and brought significant damage to lifelines (e.g., Cabinet Office Japan 2019; Takahashi and Kimura 2019). The casualties and damages were primarily related to geotechnical failures such as landslides and liquefaction (e.g., Yamagishi and Yamazaki 2018).

*Correspondence: ydhakal@bosai.go.jp
National Research Institute for Earth Science and Disaster Resilience, Tsukuba, Japan

Table 1 Coordinates of the four corners of the fault plane estimated in the present study and the hypocenter determined by JMA

Fault corners and hypocenter	Longitude	Latitude	Depth
Lower left	141.9324	42.5599	23.76
Lower right	142.0073	42.5541	41.73
Upper left	141.9666	42.8017	23.76
Upper right	142.0418	42.7959	41.73
Hypocenter	142.0067	42.6900	37.00

The earthquake was followed by many aftershocks, which concentrated primarily on a steeply dipping fault plane. Based on the spatial and temporal distribution of hypocenters of the aftershocks, a fault plane of about 28 km in length and 20 km in width was estimated. The minimum depth to the top of the fault plane was assumed to be about 24 km. The coordinates of the fault plane are provided in Table 1. The horizontal vector peak ground accelerations (PGAs) and peak ground velocities (PGVs) recorded by K-NET, KiK-net, and JMA accelerometers are plotted in Fig. 1a, b, respectively, for the mainshock.

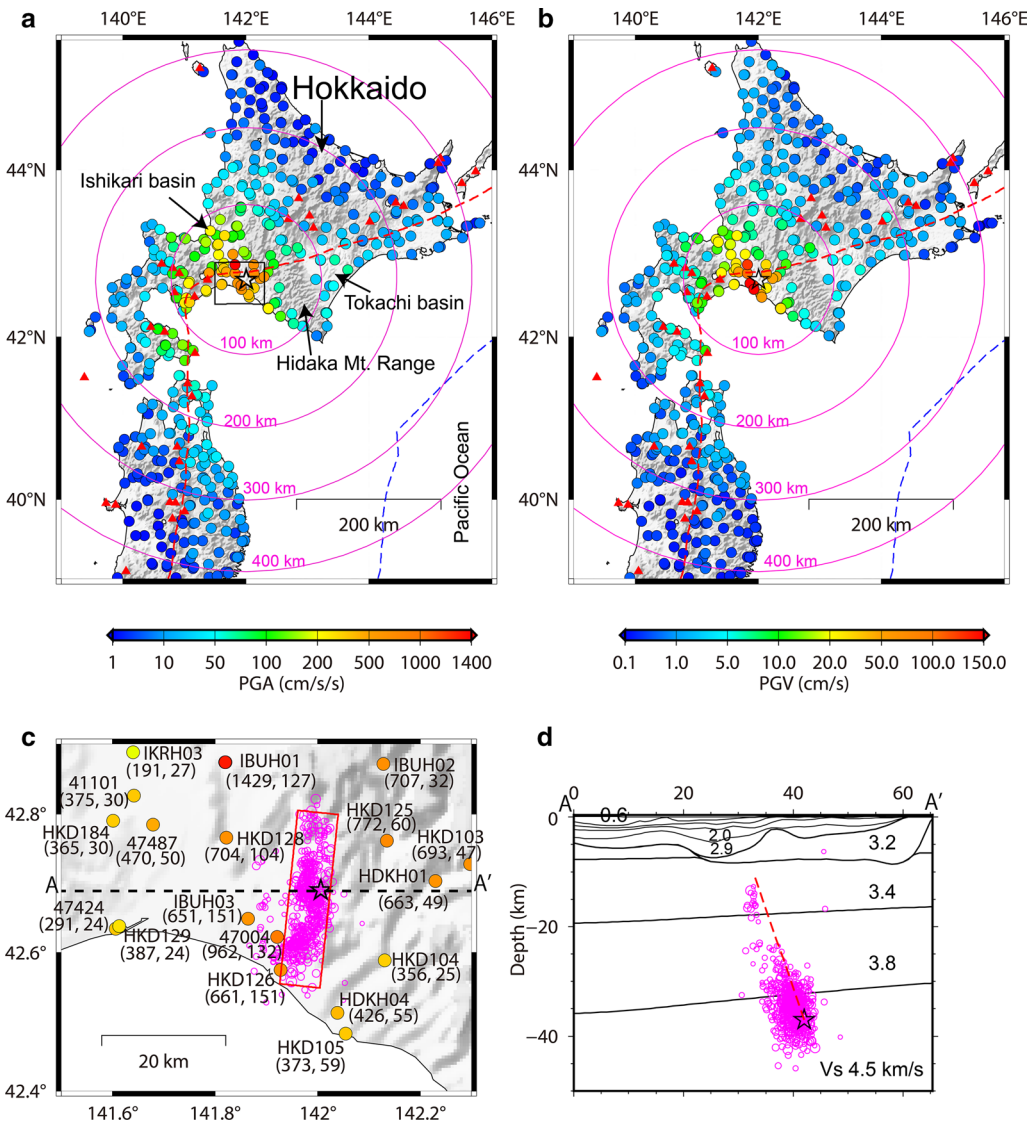

Fig. 1 **a**, **b** Show the plots of observed horizontal vector PGAs and PGVs, respectively. A star denotes epicenter of the mainshock. Triangles and dashed red line denote active volcanoes and volcanic front line, respectively. **c** Enlarged view of the rectangular area drawn around the epicenter in **a** with additional information. Numbers in parentheses denote the values of horizontal vector PGAs (cm/s^2) and PGVs (cm/s), respectively, at recording stations color-coded by PGAs. The magenta circles denote aftershocks of Mj $\geq$ 2 for the 9 days after the mainshock. The rectangle denotes the surface projection of an approximate fault plane. **d** Vertical section of JIVSM (Japan integrated velocity structure model) along the profile *A*–*A*′ shown in **c**. A red dashed line denotes the intersection line of the inferred fault plane with the vertical section

The epicenters of aftershocks and numerical values of the PGAs and PGVs at small distances from the fault are shown in Fig. 1c for the mainshock. A vertical section of the subsurface velocity model (Koketsu et al. 2012) along an east–west direction passing through the epicenter of the mainshock is drawn in Fig. 1d, which also shows the plots of depths to hypocenters of the aftershocks and the mainshock. Figure 1d shows the epicenter area covered by low-velocity sedimentary layers above the basement rocks, and the thickness of sediments is larger in the western side of the epicenter. In this paper, mainshock is used to mean the 2018 Mw 6.6 Hokkaido eastern Iburi earthquake.

The recorded maximum PGAs and PGVs for the eastern Iburi earthquake were comparable to those recorded during the 1995, Mw 6.9, Kobe earthquake (e.g., Kitagawa and Hiraishi 2004; Kawase 1996) and 2016, Mw 7.1 Kumamoto earthquake (e.g., Sakai 2016; Suzuki et al. 2017). The maximum horizontal vector PGA of 1429 cm/s^2 was observed at the KiK-net site IBUH01 (Oiwake) (see Fig. 1c). The JMA instrumental intensity (e.g., JMA 2018a, b; Shabestari and Yamazaki 2001) of 6.7 was calculated at the site IBUH01. This value of 6.7 corresponds to the upper limit of JMA intensity on a discrete scale of 0–7 (JMA 2018b). The maximum horizontal vector PGV was 151 cm/s, which was recorded at two sites: K-NET site HKD126 (Mukawa) and KiK-net site IBUH03 (Atsuma). The JMA instrumental intensity of 6.4 and 6.2 was calculated at the HKD126 and IBUH03, respectively; these values correspond to the intensity of 6 Upper in a scale of 0–7. The JMA Atsuma station (47,004 in Fig. 1c) recorded JMA instrumental intensity of approximately 6.5 (which rounds to JMA intensity of 7, the largest in the scale of 0–7). Sawazaki et al. (2006) reported that the KIK-net Atsuma site (IBUH03, see Fig. 1c for site location) experienced a strong nonlinear site response during the 2003 Mw 8.3 Tokachi-oki earthquake. We found that the nonlinear site response was most probably one of the primary causes of the large JMA intensity at the site IBUH03 during the 2018 Mw 6.6 Hokkaido eastern Iburi earthquake. We discuss in some detail the characteristics of nonlinear site response at IBUH03 in later sections. Figure 1a, b shows that the large PGAs and PGVs were observed mostly in the northwest and southeast directions of the epicenter of the mainshock and also close to the southern coastal areas at small distances (Fig. 1c), where the thickness of sediments is substantial. These observations reflect the amplification of seismic waves by the thick sediments. Moreover, as the rupture initiated nearly midway of its bottom line at a deeper portion of the fault plane and propagated along strikes and up dips, some degrees of rupture propagation effects may also be stipulated at sites close to the fault plane.

The typical characteristics of nonlinear site response are the diminution of high-frequency components of ground motions and shift of predominant frequency to lower one with respect to the linear site response (e.g., Wen et al. 1994; Satoh et al. 1995). These effects have been explained by the increase in damping and degradation of soil rigidity during strong-motions (e.g., Idriss and Seed 1968; Hardin and Drnevich 1972). Also known in the seismological and engineering communities are the atypical accelerograms, which contain large amplitude high-frequency acceleration spikes, as direct evidence of nonlinear site response during strong shakings (e.g., Holzer et al. 1989; Iai et al. 1995; Bonilla et al. 2005). These atypical accelerograms are explained as the effect of nonlinear soil response resulting from the pore water pressure changes in dilatant soils during strong shakings (e.g., Holzer et al. 1989; Iai et al. 1995). More recently, asymmetrical waveforms on vertical component accelerograms exceeding 1 g in upward direction have been described as direct evidence of nonlinear site response (e.g., Aoi et al. 2008). The asymmetric waveforms have been qualitatively explained by trampoline effect (Aoi et al. 2008) and as slap down phases (Yamada et al. 2009). During the 2018, Mw 6.6 Hokkaido eastern Iburi earthquake, we did not identify the atypical spiky accelerograms by visual inspection except a small indication on one of the horizontal components at site HKD125 (recordings not shown in this paper); however, the nonlinear site response associated with the decrease in shear modulus and increase in damping in soils was recognized at several sites, and also the asymmetrical waves on vertical components were identified at two sites. In this paper, we describe the above-mentioned nonlinear site responses during the mainshock based on observed recordings and discuss that the nonlinear site response was the most probable reason for the high-intensity ground motions at smaller distances.

The surface-to-borehole (S-to-B) spectral ratio method has been proved to be an effective method to identify nonlinear site response during strong-motions (e.g., Wen et al. 1994; Satoh et al. 1995; Sato et al. 1996; Assimaki et al. 2008; Noguchi and Sasatani 2008; Régnier et al. 2013; Kaklamanos et al. 2015; Noguchi et al. 2016). Wen et al. (2006a) introduced the horizontal-to-vertical (H-to-V) spectral ratio method to detect nonlinear site response; the method also has been widely applied in detection of nonlinear site response during strong-motions, especially when downhole recordings or rock outcrops close to the site of interest are not available (e.g., Noguchi and Sasatani 2008; Wen et al. 2011; Dhakal et al. 2017; Ren et al. 2017).

Below, we first describe the selection and processing of the data used in the present study. Then, we inquire into

the general attenuation characteristics of the observed PGAs and PGVs with distance to examine whether the peak motions are compliant with the ground motion prediction equations (GMPEs). Thirdly, we compare the S-to-B spectral ratios of S-waves for the horizontal components, i.e., horizontal-to-horizontal (H-to-H) spectral ratios for the mainshock and weak-motions from earthquakes before the mainshock at selected KiK-net sites, and discuss the characteristics of nonlinear site response at the sites. We resume the aforementioned analysis for vertical components, i.e., vertical-to-vertical (V-to-V) spectral ratios at the same sites. Then, we discuss the characteristic vertical component waveforms featuring the direct evidence of nonlinear site response during the mainshock at two KiK-net and K-NET sites. After discussing the nonlinear site effects on horizontal and vertical component recordings, we present the H-to-V spectral ratios from surface recordings at the KiK-net sites where S-to-B spectral ratios are analyzed. We compare the results between the S-to-B and H-to-V spectral ratios at the KiK-net sites. We also analyze the H-to-V spectral ratios at selected K-NET sites. Finally, based on the analyses above and comparisons, we conclude by an ad hoc equation to take account of the nonlinear site amplification into an existing GMPE for PGVs.

Data selection and processing

Strong-motion seismometers of K-NET and KiK-net recorded ground motion data of mainshock at more than 475 stations and epicentral distances between about 10 and 900 km. Similarly, strong-motion data recorded by JMA intensity meters at 142 stations that spread for 700 km were made available by JMA. The PGAs and PGVs were calculated from the high-pass-filtered strong-motion seismograms with a cutoff frequency of 0.07 Hz. In this paper, the PGAs and PGVs refer to the maximum values of the vector sum (i.e., the square root of the sum of squares) of two horizontal component acceleration and velocity time histories, respectively, over the available time steps. We did not show PGAs and PGVs at large distances in Figs. 1 and 2 because of their small values. Attenuation relation by Si and Midorikawa (1999, 2000) has been the basis for seismic hazard evaluation in Japan (e.g., Fujiwara et al. 2009). They defined peak value in their equation as larger one of the two horizontal components. Therefore, when we compared the peak values with the attenuation relation by Si and Midorikawa (1999, 2000) in Fig. 2, we adhere to their definition. The fault distance to use in their equation was determined from the fault geometry model briefly mentioned in the previous section. The fault geometry model was estimated based on the automatically determined hypocenters provided by JMA (see Availability of data and materials). The geographical coordinates of the four corners of the fault model with depths at the corners are given in Table 1. The aftershocks of $Mj \geq 2$ that occurred within 9 days were used. In Fig. 1c, d, 460 aftershocks of Mj between 2.0 and 2.9, 136 aftershocks of Mj between 3 and 3.9, 37 aftershocks of Mj between 4.0 and 4.9, and two aftershocks of Mj equal to 5.4 and 5.5 were plotted.

The sites used for analysis of nonlinear characteristics are portrayed in Fig. 3; the total number of sites is 32. The KiK-net sites consist of a pair of surface and borehole sensors, and recordings from 16 KiK-net sites that recorded horizontal vector PGAs of about 70 cm/s^2 or larger at the surface and 20 cm/s^2 or larger at boreholes were analyzed. The K-NET sites consist of sensors at the surface only, and recordings from 16 K-NET sites that recorded horizontal vector PGAs of 200 cm/s^2 or larger were analyzed. The Vs30 values (average S-wave velocities in the upper 30 m of the soil column) (e.g., BSSC 2003) are often used to define site condition. We obtained the Vs30 values at the KiK-net sites from NIED (see Availability of data and materials). Most of the K-NET sites have PS-loggings down to 10–20 m. We obtained the Vs30 values at the K-NET sites having PS-loggings down to 20 m by using the correlation formula between Vs30 and Vs20 derived by Kanno et al. (2006). At sites where Vs20 was not available, we obtained the Vs10 values for information. The PGAs, PGVs, and Vs10 or Vs30 values at the KiK-net and K-NET sites are listed in Tables 2 and 3, respectively. The shallow soil Vs values were not available at the JMA sites, and hence, the analysis of nonlinear site response was limited to the K-NET and KiK-net sites in this paper.

We selected recordings which contained both the P- and S-waves to assist in picking the onset of S-waves. The onset of S-waves was handpicked, and a time window of 10 s was used to compute Fourier spectral amplitudes. As a preliminary analysis, we also computed the Fourier spectral amplitudes from a time window of 15 s and compared them from the time window of 10 s. The two results were essentially identical at frequencies of our interest between 0.5 and 20 Hz. However, to avoid the possible effects of 3-D subsurface structure on computed spectra due to a long-time window (e.g., Dhakal and Yamanaka 2012), we limited the S-wave time window of 10 s in our analysis. The 10-s time window was also optimal to evaluate the signal-to-noise ratio considering the stability of the computed spectra as the recordings had pre-event noise time windows smaller than 15 s. In the actual calculation, the mean acceleration of the noise time window was subtracted from the whole recordings as a baseline correction. Then, cosine tapering of 1 s was applied just outside of the selected S-wave time window of 10 s at both ends, i.e., the 10-s time window

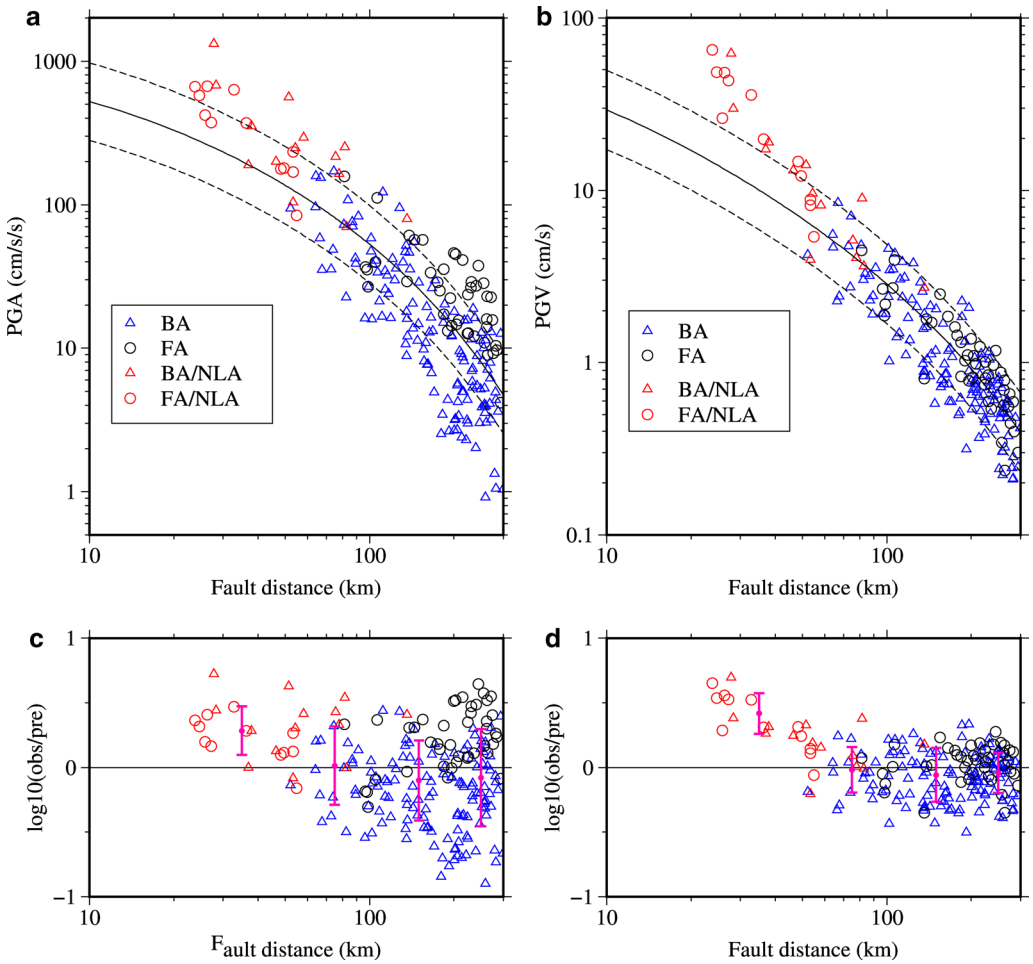

Fig. 2 **a**, **b** Plots of observed PGAs (larger of two horizontal components) and PGVs (larger of two horizontal components) after adjustment for site amplification, respectively. Only a subset of data shown in Fig. 1a were plotted where the values of Vs30 were known or estimated. The solid lines represent median prediction curves using equations in Si and Midorikawa (1999, 2000) for Mw = 6.6, depth = 37, and type of event = crust, and dashed lines denote plus–minus one standard deviation. In the legends, BA, FA, and NLA are the abbreviations for back-arc, fore-arc, and nonlinear site response analyzed sites. **c**, **d** Plots of residuals for the PGAs and PGVs plotted in **a**, **b**, respectively. Mean residuals with a plus–minus one standard deviation are shown by vertical bars for four different distance ranges 20–50 km, 50–100 km, 100–200 km, and 200–300 km

becomes 12 s with the addition of 1-s time window for tapering at each end. Then, 20 s of zeroes was padded, so the length of the time window is 32 s. The Fourier spectral amplitudes were smoothed by applying a Parzen window of 0.4 Hz. The recordings were selected if the Fourier spectral ratios between the S-waves and noise window were greater than three at all frequencies between 0.5 and 20 Hz. The weak-motion recordings were obtained from events that occurred within 300 km of each site between 1996 and the day before the mainshock and were recorded by K-NET and KiK-net. The magnitudes of the events ranged mostly between Mj 4.0 and 6.5. In this paper, the weak-motion recordings mean those recordings having horizontal vector PGAs between 5 and 20 cm/s^2 at the surface. A few recordings had PGAs lower than 5 cm/s^2 or greater than 20 cm/s^2 but lower than 30 cm/s^2 to increase the number of recordings. The number of recordings varied from site to site and ranged between 10 and 130 (see Tables 2, 3). For the mainshock recordings, the beginning of S-wave time window for analysis was selected based on the dominant wave packet for S-waves. The Fourier spectral amplitudes for vertical components also were computed from the time windows same as horizontal component S-wave time windows for the both weak-motions and mainshock. The smoothing operation was also identically applied. An example of S-wave time windows for weak- and strong-motions is depicted for site IBUH01 in Fig. 4. The site IBUH01 is the

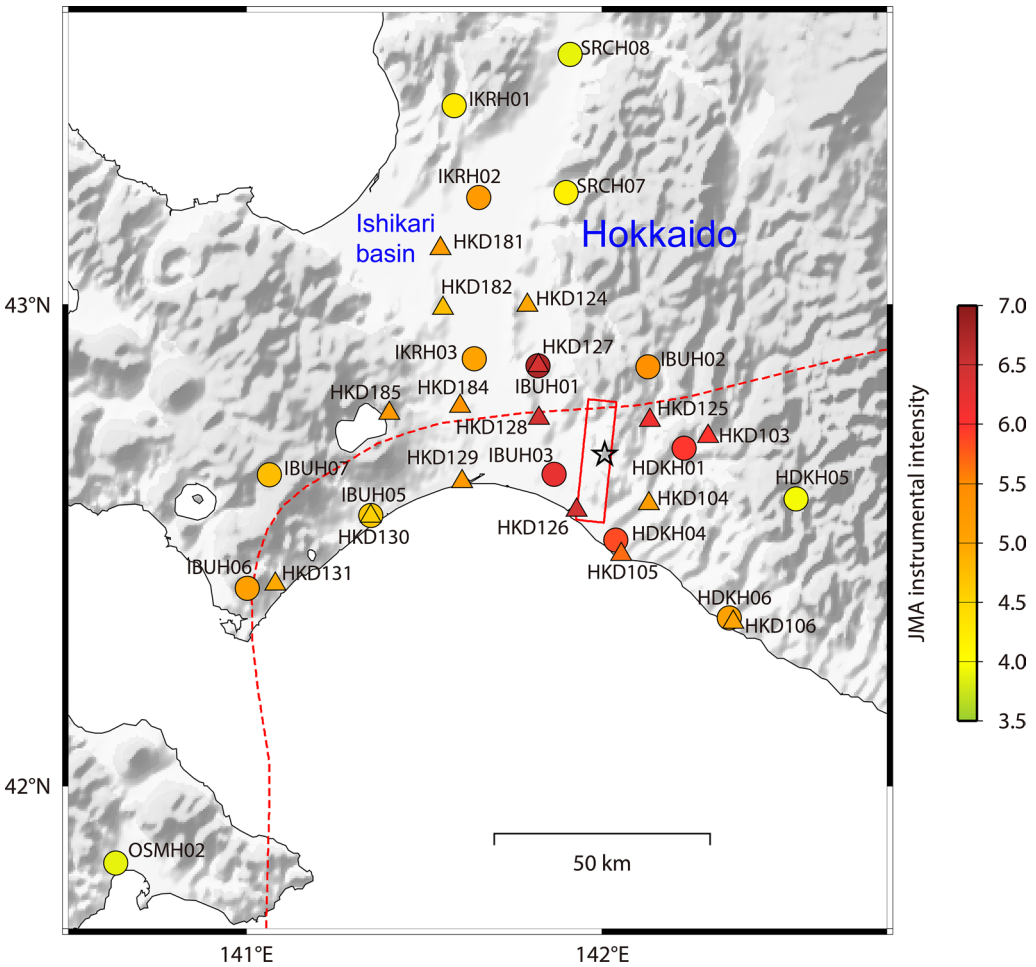

Fig. 3 Location of sites used in the evaluation of nonlinear site response. The K-NET and KiK-net sites are denoted by triangles and circles, respectively. The site codes are written next to the site symbols, which are color-coded by the JMA instrumental intensity. A star denotes epicenter of the mainshock, and rectangle denotes surface projection of the fault plane. A dashed red line denotes volcanic front (see also Fig. 1). See Tables 2 and 3 for various parameters at each site

site that recorded the largest PGA during the mainshock as described in the previous section.

Comparison of PGAs and PGVs

Si and Midorikawa (1999) developed attenuation relations for PGAs on soil sites. They proposed a factor of 1.4 to convert the PGAs at rock sites to PGAs at soil sites. However, the objective definition of rock and soil was not available in their paper. They referred to the paper by Joyner and Boore (1981) for the definition of site condition. Joyner and Boore (1981) classified sites into two groups: rock and soil based on geological information. They described in another paper (Boore and Joyner 1997) Vs30 value of 620 m/s for generic rock sites in western North America. In the National Earthquake Hazards Reduction Program (NEHRP) recommendations (BSSC 2003; NEHRP 2019), sites having Vs30 value of 760–1500 m/s and higher than 1500 m/s are classified as rock and hard rock sites, respectively. In line with the literature mentioned above, we considered a site having Vs30 value of 760 m/s or larger as a rock site and a site having Vs30 value otherwise as a soil site. None of the sites at small fault distances have Vs30 values between 620 and 760 m/s in our data set. Therefore, selecting site class definition based on Joyner and Boore (1981) or NEHRP recommendations does not make a difference to our conclusions in this paper. We multiplied the PGAs at rock sites by 1.4 as aforementioned and plotted together with other soil sites in Fig. 2a; the prediction curves in Fig. 2a are for soil site condition. In the figure, the back-arc and fore-arc sites, separated by a volcanic front line, are denoted by triangles and circles, respectively. Red color symbols indicate the sites used in the nonlinear analysis. In the figure, it can be seen that the observed

Table 2 List of KiK-net sites with site parameters, peak ground motions, and nonlinear site response indices

ID	Site	*R* (km)	Vs30	Surface				Borehole				DNL			F_s (Hz)			F_w (Hz)			int	N
				HPGA (cm/s/s)	HPGV (cm/s)	UD PGA (cm/s/s)	UD PGV (cm/s)	HPGA (cm/s/s)	HPGV (cm/s)	UD PGA (cm/s/s)	UD PGV (cm/s)	S/B	H/V	V/V	S/B	H/V	V/V	S/B	H/V	V/V		
a	IBUH01	27.8	307	1429.2	127.0	1062.0	36.8	259.4	17.4	84.3	5.9	6.8	10.9	5.5	1.97	2.22	4.06	9.56	5.81	17.13	6.74	130
b	IBUH02	28.3	542	707.3	31.7	139.0	5.8	128.3	15.0	51.9	5.8	5.8	6.7	2.8	7.22	7.78	16.16	11.75	10.34	16.91	5.41	15
c	HDKH01	32.8	368	663.4	48.9	316.8	15.0	119.2	17.4	85.2	8.2	4.7	6.2	3.8	3.22	3.94	5.94	8.56	6.47	18.38	5.97	49
d	IBUH03	24.7	111	650.9	150.7	701.5	25.6	794.7	38.8			11.7			0.5	0.5		1.91	0.81		6.23	50
e	HDKH04	25.8	235	425.7	55.4	196.8	9.4	162.9	25.5	80.2	5.6	6.8	7.2	2.2	0.88	1.09	15.84	11.66	7.03	19.72	5.86	49
f	IKRH02	58.1	128	299.2	22.6	74.8	3.7	126.5	6.0	20.8	2.1	3.9	3.6	2.5	2.09	2.81	3.19	3.78	2.53	5.41	5.21	15
g	IBUH05	53.4	379	266.0	11.6	129.4	4.4	112.5	7.4	36.4	3.2	4.9	4.4	2.7	12.03	3.44	18.94	14.47	2.66	19.63	4.66	29
h	IBUH06	81.7	305	260.1	14.4	202.6	7.0	54.0	2.0	25.9	1.6	7.1	3.5	5	1.91	1.84	4	2.97	2.22	4.25	5.13	63
i	IBUH07	75.6	259	222.2	9.8	81.6	3.4	67.1	3.3	35.3	1.5	4.2	4.3	4.1	2	5.63	12.28	2.09	1.84	2.72	4.76	23
j	HDKH06	48.2	412	195.7	21.1	107.0	7.4	45.8	9.5	33.8	4.9	2.5	2.2	3.3	2.56	2.25	4.97	1.78	1.47	4.84	5.07	113
k	IKRH03	37.0	326	190.6	26.9	102.0	4.5	135.3	11.6	51.5	3.4	6.1	6.1	3	2.41	2.09	8.63	7.09	2.59	12.19	5.03	65
l	IKRH01	77.9	405	164.9	6.7	42.3	2.9	44.0	2.8	18.8	1.8	1.5	2.5	2.4	4.41	10.66	7.34	14.09	16.41	12.13	4.26	46
m	SRCH07	53.4	316	104.0	6.8	50.3	2.8	21.4	3.6	20.1	2.4	2.3	2.2	2.2	6.75	7.31	10.09	3.84	4.75	8.91	4.2	40
n	OSMH02	135.9	325	80.9	4.5	22.9	1.5	30.0	1.9	9.1	1.3	2.7	2.6	2.4	3.81	0.88	13.59	2.81	2.69	11.91	3.88	18
o	SRCH08	82.6	347	73.6	5.4	29.6	2.6	22.0	2.9	15.3	2.1	5.1	2.7	2.7	6.63	5.78	10.47	4.56	5.94	11.75	3.89	47
p	HDKH05	54.9	766	67.7	5.4	27.9	2.5	26.0	4.5	23.6	3.4	3.8	4.9	2.2	7.66	6.81	8.41	8.63	6.22	10.19	3.95	54

The first column with header ID marks the identification of each panel in Figs. 5, 7, and 12

R fault distance; Fs and Fw predominant frequencies of strong- and weak-motions, respectively; HPGA horizontal vector PGA; HPGV horizontal vector PGV; int JMA instrumental intensity calculated in this study; N number of weak-motion recordings used to compute the mean spectral ratios. For other headers, see the text

Table 3 List of K-NET sites with site parameters, peak ground motions and nonlinear site response indices

ID	Site	*R* (km)	Vs30 (m/s)	HPGA (cm/s/s/)	HPGV (cm/s)	UD PGA (cm/s/s)	UD PGV (cm/s)	DNL	Fw (Hz)	Fs (Hz)	int	*N*
a	HKD127	27.8	189*	1317.8	95.6	1592.6	45.0	13.1	7.78	2.06	6.41	54
b	HKD125	27.6	129*	772.0	60.3	202.9	14.7	3.3	2.47	1.53	6.14	26
c	HKD128	26.3	192	704.0	104.3	396.5	27.1	4.7	1.47	1.25	6.44	60
d	HKD103	36.5	174*	693.1	46.9	344.0	17.2	6.1	6.84	2.09	5.98	17
e	HKD126	23.8	166	661.4	151.4	334.9	13.8	13.4	3.06	0.53	6.45	36
f	HKD124	35.3	287*	624.6	22.0	120.0	5.1	6.8	12.5	8.44	4.99	13
g	HKD185	51.4	311	561.7	21.5	325.3	6.3	3.4	1.56	1.41	5.25	79
h	HKD129	36.3	438	386.8	24.1	126.0	7.0	4.9	0.84	3.38	5.25	18
i	HKD105	27.2	375	373.3	58.7	320.3	17.1	6.8	4.94	1.09	5.68	59
j	HKD184	37.9	293	365.4	30.4	448.5	10.8	4.4	4.22	3.47	5.34	56
k	HKD104	28.6	243*	355.6	25.5	113.9	6.6	3	5.38	6.84	5.17	13
l	HKD131	75.4	266*	353.9	11.5	166.4	4.6	4.6	8.25	7.72	4.97	37
m	HKD181	54.4	221	277.9	18.4	117.3	6.9	3.8	0.75	0.5	5.18	24
n	HKD130	53.3	455	205.8	11.4	127.5	4.5	3.1	2.59	3.44	4.57	14
o	HKD182	46.4	311	205.1	20.0	107.4	3.2	2.6	4.06	4.34	4.76	10
p	HKD106	49.4	245	201.9	23.7	41.2	5.2	2.6	4.75	1.91	5.03	28

The first column with header ID marks the identification of each panel in Fig. 14. *R*, fault distance; the numerals marked with * under the header Vs30 are the values of Vs10 at the corresponding sites

HPGA horizontal vector PGA; HPGV horizontal vector PGV; Fw and Fs predominant frequencies of strong- and weak-motions, respectively; N number of weak-motion recordings used; int JMA instrumental intensity calculated in this study. For other headers, see the text

values are generally larger than the median predictions between 20 and about 50 km while the values do not show any visible trend at distances over about 50 km for a reasonable range of scattering. It can also be seen that the observed values at back-arc sites are systematically smaller than the values at the fore-arc sites at distances over about 100 km, which can be recognized in the plots of residuals in Fig. 2c. The mean residuals in base-10 log-scale are approximately 0.28, 0.01, −0.10, and −0.08 for binned data between 20 and 50 km, 50 and 100 km, 100 and 200 km, and 200 and 300 km, respectively. The above results suggest that despite the difference between the fore-arc and back-arc data, the absolute values of the mean residuals at the longer distances are smaller than those at smaller distances.

A comparison of the observed PGVs with the empirical attenuation relation by Si and Midorikawa (1999) is shown in Fig. 2b. Unlike the PGAs, attenuation relation for PGVs was developed for a stiff site condition having Vs30 value of about 600 m/s. They adjusted the observed PGV at a site by a factor that is a function of Vs30 value at the site using the equation in Midorikawa et al. (1994). We followed the same procedure and adjusted the observed PGVs for site amplification effect. The adjusted observed values are plotted in Fig. 2b together with the prediction curves for stiff site condition having Vs30 value of 600 m/s. Similar to the PGAs discussed above, the observed PGVs are generally larger than the median predictions at distances smaller than about 40 km and are similar to the predictions at distances over about 40 km for a reasonable range of scattering. The distribution of residuals between the observed and predicted PGVs is plotted in Fig. 2d as a function of fault distance. The mean residuals in base-10 log-scale are approximately 0.42, -0.02, -0.06, and -0.04 for binned data between 20 and 50 km, 50 and 100 km, 100 and 200 km, and 200 and 300 km, respectively. The remarkably smaller mean residuals at distances beyond 50 km confirm that the observed PGVs at those distances are similar from the typical crustal earthquakes in Japan. On the other hand, the large positive mean residual at smaller distances point toward some specific causes or combination thereof not sufficiently addressed by the GMPEs.

One notable difference between the plots for PGAs and PGVs is that the PGVs scatter less from the median predictions than the PGAs at longer distances, and the difference between the back-arc and fore-arc sites becomes smaller for PGVs. These results are generally desirable because the relatively long-period ground motions become less sensitive to very shallow earth structures compared to the short-period ground motions. Dhakal et al. (2010) reported that the distinction of fore-arc and back-arc data becomes less obvious at periods larger than about 0.5 s. In summary, the observed PGAs and PGVs were generally described very well by the attenuation relations in Si and Midorikawa (1999) at distances larger than about 50 km. In this paper, we are, therefore, primarily interested

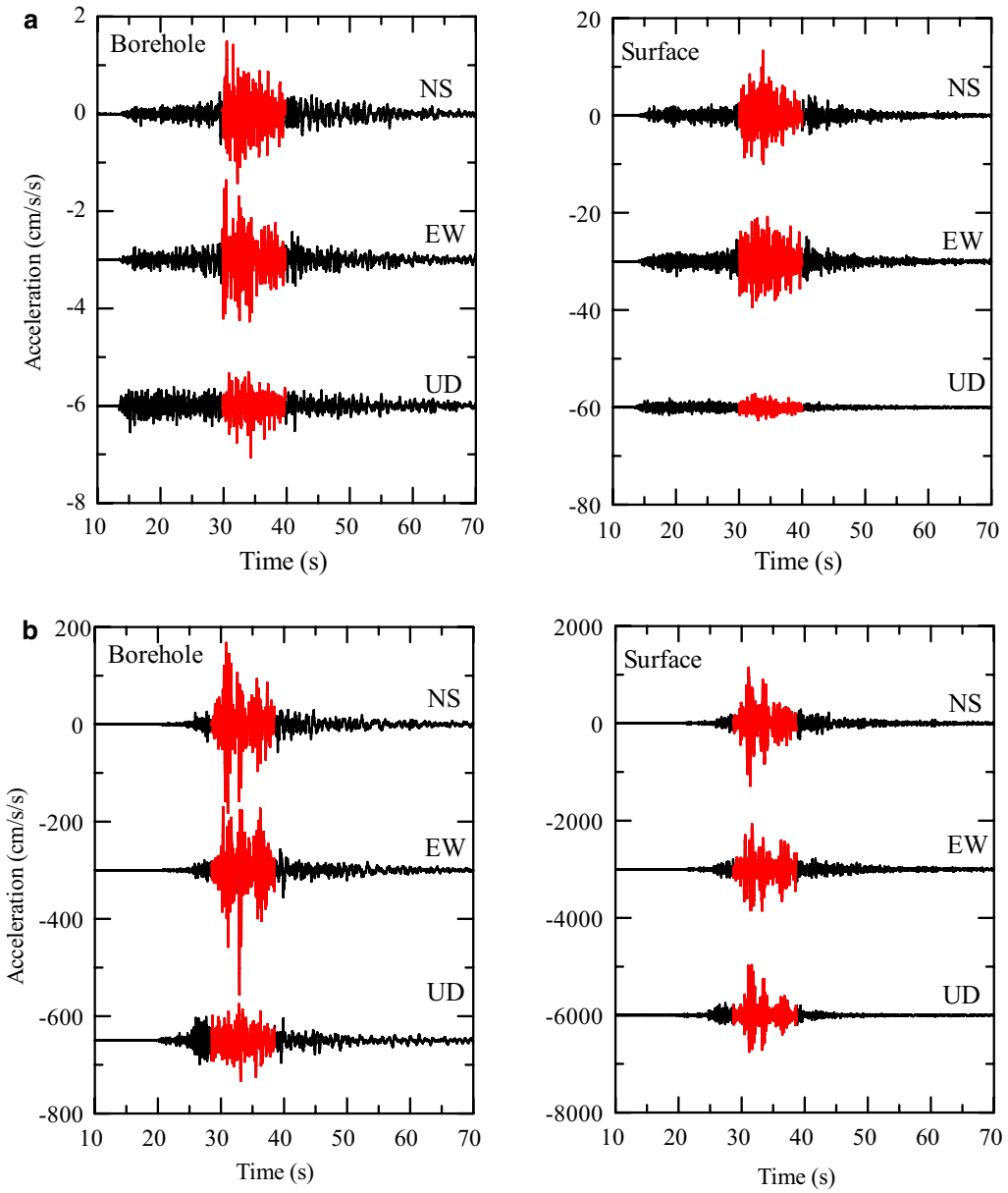

Fig. 4 Example acceleration recordings and S-wave time windows (red portions) selected for evaluation of nonlinear site response at site IBUH01. **a** Recordings from an event that occurred on Nov 1, 2006, at 23:21 JST (Mj = 4.8, focal depth = 49 km, epicentral distance = 123 km, back azimuth = 120°). **b** Recordings from mainshock. The borehole and surface recordings are plotted in left and right panels, respectively. The north–south (NS), east–west (EW), and vertical (UD) components are indicated in each panel. Note that the scale of the vertical axis for surface recordings (right panels) is larger by a factor of 10 with respect to that for borehole recordings. The recordings for the mainshock are shifted to the right by 4 s to match with the S-wave arrivals on the weak-motion recordings in panel **a**

in sites of large residuals between the observed and predicted PGVs at smaller distances. We explore the observed characteristics of nonlinear site response at the selected KiK-net and K-NET sites mostly from the smaller distances in the next four sections.

S-to-B spectral ratios of horizontal components

In this study, we obtained S-to-B spectral ratios of horizontal components (H-to-H) in the following way. We calculated the Fourier spectral amplitudes for each horizontal component, smoothed them as explained in the

data processing section, obtained the vector sum of two components at each frequency, and calculated the ratios between the surface and borehole spectra at each frequency. Wen et al. (2006b) proposed the following equation (Eq. 1) to express the deviation of H-to-V spectral ratios of the strong- and weak-motions quantitatively:

$$d(f) = \frac{s(f) - w(f)}{\sigma(f)} * 100\% \quad (1)$$

where $s(f)$ is the H-to-V spectral ratios of the strong-motions, $w(f)$ is the mean H-to-V spectral ratios of the weak-motions, and $\sigma(f)$ is the standard deviation of the H-to-V spectral ratios of the weak-motions at frequency f. This method gives more than a single value of degree of nonlinearity (DNL) because it is calculated for each frequency. Wen et al. (2006b) suggested averaging the values at multiple frequency bands because the nonlinear effects may be stronger at certain frequencies than the others. In this study, we calculated the DNL value using Eq. 2, which was first employed by Noguchi and Sasatani (2008):

$$\mathrm{DNL} = \sum \left| \log \left\{ \frac{R_{\mathrm{strong}}}{R_{\mathrm{weak}}} \right\} \right| \Delta f \quad (2)$$

where R_{strong} and R_{weak} represent the spectral ratios for strong- and weak-motions, respectively, and Δf is the frequency interval. The DNL value was obtained from spectral ratios between 0.5 and 20 Hz in Noguchi and Sasatani (2008, 2011). We also used the same frequency range for the computation of DNL values in this paper. One of the advantages of this DNL index is that it gives a single value that facilitates the comparison with other parameters like PGA. Equation 2 may be considered as a variant of Eq. 1 and was used in several previous studies. Interested readers can find further variants of Eq. 2 in Régnier et al. (2013) and Ren et al. (2017).

Another important parameter that has been used to describe the effect of nonlinear site response is the amount of shift of predominant frequencies of site response during strong-motions as mentioned above. In this paper, we make use of both indices, DNL and shift of predominant frequencies, in the discussion of the characteristics of nonlinear site response during the mainshock. In this paper, predominant frequency means the frequency that corresponds to the peak spectral ratio between 0.5 and 20 Hz.

The S-to-B spectral ratios at 16 KiK-net sites are plotted in Fig. 5 in the order of decreasing horizontal vector PGA from top-left to bottom-right panels a to p, respectively. The spectral ratios for the mainshock at the first five sites, panels a to e, namely IBUH01, IBUH02, HDKH01, IBUH03, and HDKH04, corroborated the two most well-known features of nonlinearity: the reduction in high-frequency components and shift of predominant frequency toward lower one during the strong-motions. The DNL values were between 4.7 (at HDKH01, Fig. 5c) and 11.7 (at IBUH03, Fig. 5d). The predominant frequencies of the sites were reduced by approximately 38% (at IBUH02, Fig. 5b) to 92% (at HDKH04, Fig. 5e). It can be seen that the site IBUH03 (Fig. 5d), which attained the largest DNL, was largely depleted in high-frequency components. We found that the reduction in peak frequency at the site IBUH03 was approximately 73% during the mainshock in comparison with the weak-motions (from 1.9 to ~ 0.5 Hz). This result at the site IBUH03 is commensurate with the reduction in peak frequency by 50% (from 1.2 to 0.6 Hz) reported in Sawazaki et al. (2006) during the 2003 Mw 8.3 Tokachi-oki earthquake. The smaller value of the peak frequency (~ 0.5 Hz) in this study may be due to the much stronger input motions at the site during the 2018 Mw 6.6 earthquake (surface PGA of ~ 651 cm/s^2) compared to that during the 2003 Mw 8.3 Tokachi-oki earthquake (surface PGA of ~ 376 cm/s^2). We note that the peak frequencies of weak-motions are slightly different between this study and Sawazaki et al. (2006); this may be due to the difference in the data set of weak-motions being used in the respective analyses. We obtained the peak frequency from S-wave portions of the small events while Sawazaki et al. (2006) obtained the values from coda waves. The next six sites, panels f to k in Fig. 5, namely IKRH02, IBUH05, IBUH06, IBUH07, HDKH06, and IKRH03, mostly showed the reduction in higher-frequency components; the DNL values ranged between 2.5 and 7.2. The spectral ratios at IKRH01 (Fig. 5l), SRCH07 (Fig. 5m), and OSMH02 (Fig. 5n) were very similar between the mainshock and weak-motions, suggesting for a little or no nonlinearity; the DNL values at the sites were between 1.5 and 2.7. The remaining two sites, namely SRCH08 (Fig. 5o) and HDKH05 (Fig. 5p), showed the reduction in higher-frequency components primarily; the DNL values were 5.1 and 3.8, respectively. The observed features of spectral ratios and the DNL values described above confirmed that the threshold DNL value of 2.5 suggested by Noguchi and Sasatani (2011) was generally robust to identify nonlinear site response using the S-to-B spectral ratios of S-waves. The results discussed above are summarized in Table 2.

It is often presumed that one of the reasons for the smaller variance of PGAs at short distances is due to soil nonlinearity because the nonlinearity averages out the amplifications at soft sites to that at stiff sites at high-frequency components (e.g., Midorikawa and Ohtake 2004). The observed spectral ratios at the site IBUH01 manifested the reduction in the spectral ratios at frequency components higher than about 3 Hz during the

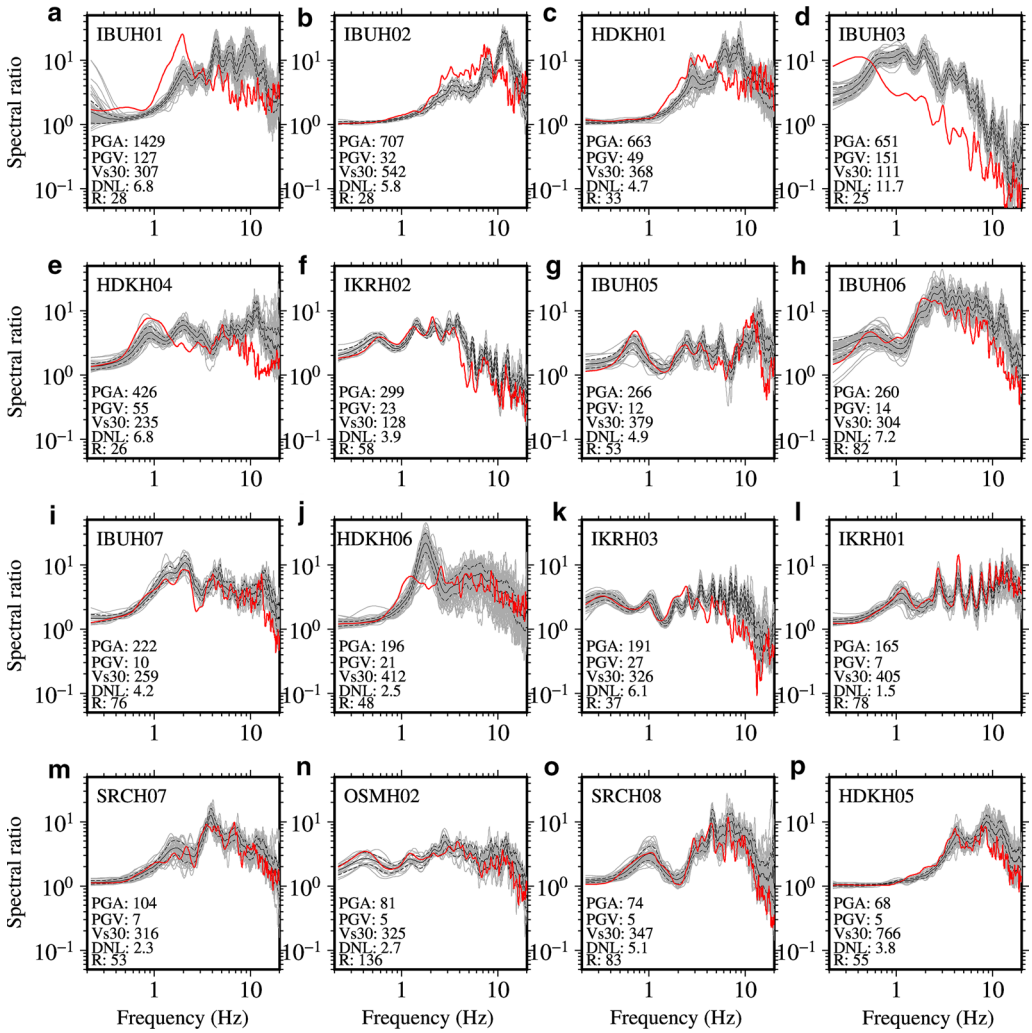

Fig. 5 Comparison of surface-to-borehole spectral ratios of horizontal component recordings during weak-motions (gray lines) and those during the mainshock (red lines) at KiK-net sites. The plots are arranged in order of decreasing horizontal vector PGAs in panels **a**–**p**, respectively. Solid black lines denote mean spectral ratios for weak-motions, and dashed gray lines denote one standard deviation. The PGA in units of cm/s^2, PGV in units of cm/s, Vs30 in units of m/s, DNL values, and fault-to-site distance (*R*) in units of km are also included for each site. See Fig. 3 for site locations

mainshock compared with those during the weak-motions (see Fig. 5a). At the same time, an increase in spectral ratios occurred between about 1 and 3 Hz. We compared the surface and borehole NS component recordings at two different passbands (0.5–3 Hz and 3–10 Hz) at the site IBUH01 in Fig. 6a for an event of Mj 4.8, an epicentral distance of 123 km, and focal depth of 49 km. It can be seen that the PGAs are larger for both the borehole and surface recordings in the passband of 3–10 Hz than the values in the passband of 0.5–3 Hz. The S-to-B ratio of PGAs in the passband of 0.5–3 Hz is approximately three while the ratio is approximately 11 in the passband of 3–10 Hz; the amplification of PGAs in the two passbands is in line with the spectral ratios for weak-motions. The borehole and surface NS component recordings during the mainshock are drawn in Fig. 6b. The borehole recording had the larger PGA in the passband of 3–10 Hz than that in the passband of 0.5–3 Hz; this feature was identical with the weak-motions shown in Fig. 6a. On the contrary, the observed PGA at the surface was much larger in the passband of 0.5–3 Hz than that in the passband of 3–10 Hz. The S-to-B PGA ratios were approximately 11 and 4 in the 0.5–3 Hz and 3–10 Hz passbands, respectively. The above results were very similar between the borehole and surface recordings for the EW components as well. In regions of high intensity, Midorikawa and Fukuoka (1988) found that the lower frequency motions with a frequency of around

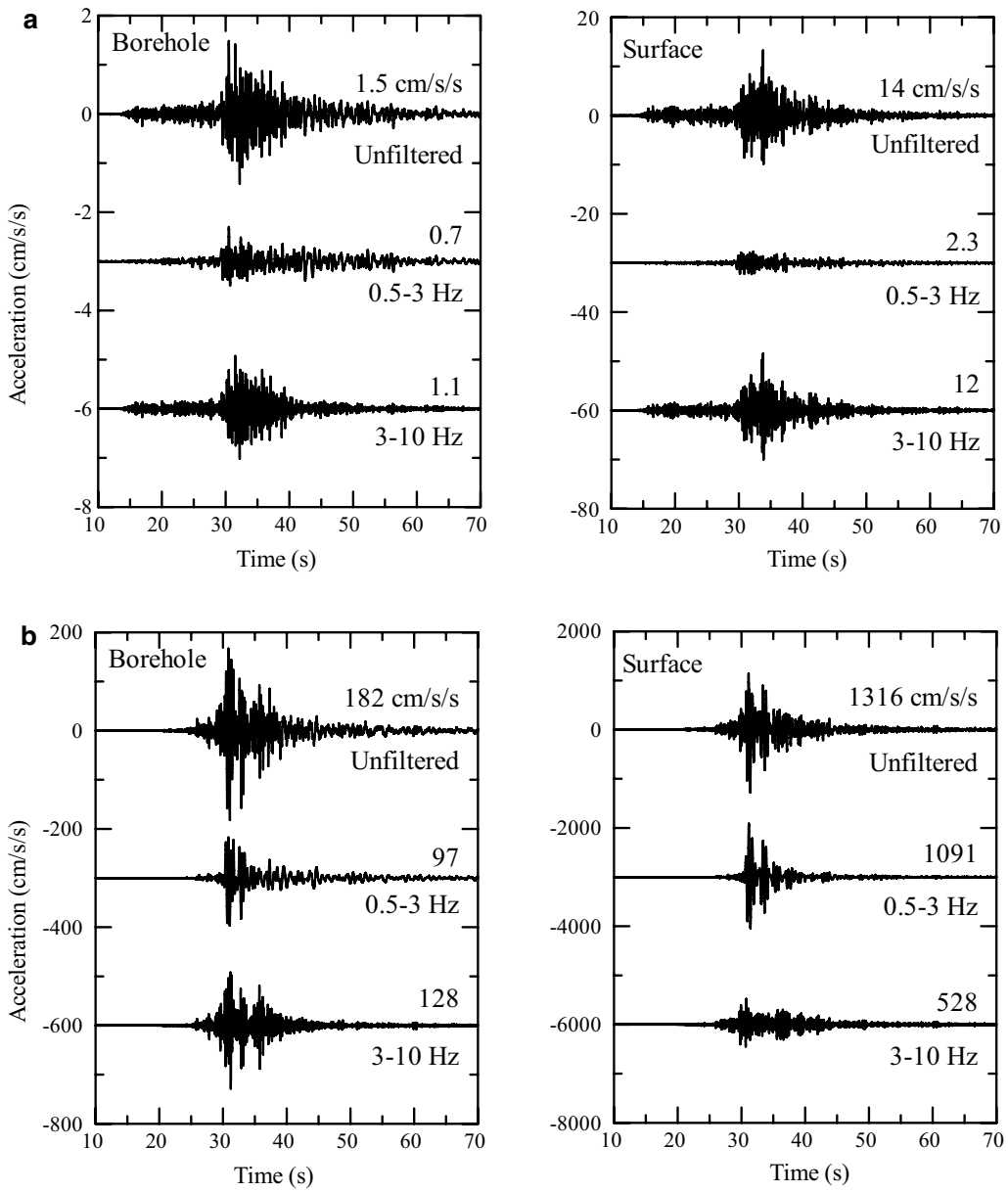

Fig. 6 Comparison of the borehole (left panel) and surface (right panel) NS component acceleration recordings for weak-motions (**a**) and mainshock (**b**) at site IBUH01 at different passband frequencies. The weak-motion recordings are from an event that occurred on November 1, 2006, at 23:21 JST (Mj = 4.8, focal depth = 49 km, epicentral distance = 123 km, back azimuth = 120°). In each panel, the uppermost recordings are unfiltered ones; the middle and lowermost recordings were bandpass filtered at 0.5–3 Hz and 3–10 Hz, respectively, as indicated in each plot. The maximum acceleration in the unit of cm/s^2 is indicated above each trace. Note that the scale of the vertical axis in the right panels is larger by a factor of 10 with respect to that in left panels

2 Hz had a higher correlation with the JMA intensities. As shown in Fig. 4b, the vertical component recording had PGA larger than 1 g at the site IBUH01. However, we confirmed by calculation of the JMA intensity with and without the vertical component recording that the influence of vertical component recording was negligible on the reported intensity (6.74 vs 6.67). The above analysis confirmed that the large increase in amplification factors due to nonlinearity resulted in the largest JMA intensity at the site IBUH01. It is somewhat difficult to notice from only the spectral ratios that the nonlinear site response resulted in the large intensities at short distances such as at the sites IBUH03 and HKD126 because the sites are located up-dip and in the direction

of rupture propagation (see Fig. 3). Indeed, the source-type effect that may be forward rupture directivity was recognized at the two sites. Because the site IBUH03 recorded horizontal components of ground motions both on the surface and at the borehole, we presented somewhat detail comparison of the amplification of the PGVs at different frequency bands for a small event and the mainshock in an Additional file 1. The analysis indicated that the nonlinear site amplification at the top of the large input motions caused one of the largest PGVs during the mainshock beyond the predominant frequency of linear site amplification. Examples of similar phenomena from the near field recordings may be found in Bray and Rodriguez-Marek (2004) and Garini et al. (2017). These observations suggested that the nonlinearity does a favor by reducing amplitudes of some frequency components but at the cost of increasing the strength of ground motions at other frequencies during strong-motions. We discuss the characteristics of nonlinear site response on the vertical components in the next two sections.

S-to-B spectral ratios of vertical components

The S-to-B spectral ratios of vertical components (V-to-V) for the mainshock and weak-motions are plotted in Fig. 7 at all sites described in the previous section except at the site IBUH03, where the vertical component

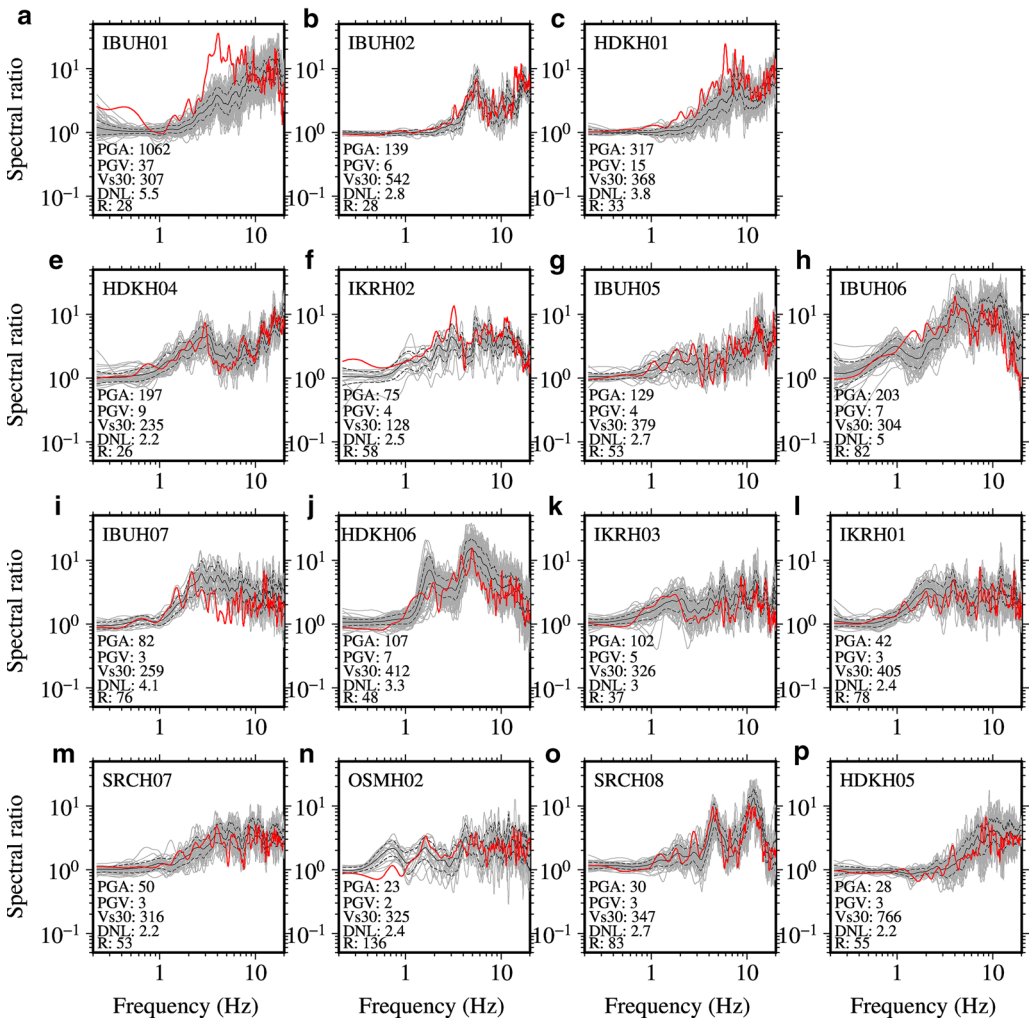

Fig. 7 Comparison of surface-to-borehole spectral ratios of vertical component recordings during weak-motions (gray lines) and those during the mainshock (red lines) at KiK-net sites. The plots are arranged in order of the sites plotted in Fig. 5 (i.e., decreasing horizontal vector PGAs from top-left **a** to bottom-right **p** panels). Solid black lines denote mean spectral ratios for weak-motions and dashed gray lines one standard deviation. The vertical PGA in units of cm/s^2, vertical PGV in units of cm/s, Vs30 in units of m/s, DNL values, and fault-to-site distance (R) in units of km are also included for each site. Note that the plot for site IBUH03 is not available due to malfunction of the vertical component instrument at underground. See Fig. 3 for site locations

borehole sensor did not record the shakings correctly. The sites in Fig. 7 are arranged in the same order as those plotted in Fig. 5. The DNL values were obtained using Eq. 2. Our results described shortly indicated that the DNL value of 3.5 or larger may indicate nonlinear site response on vertical components. The threshold value is very similar to the threshold value of 4 suggested by Noguchi and Sasatani (2011) to identify nonlinear site response on horizontal components using the H-to-V spectral ratios.

The site IBUH01 (Fig. 7a) exhibited a remarkable shift of peak spectral ratios and considerable amplifications at frequencies between about 3 and 6 Hz during the mainshock compared with those during the weak-motions. The DNL value was 5.5, and the reduction in peak frequency was approximately 76% (from 17.13 to 4.06 Hz). This site recorded vertical ground acceleration exceeding 1 g at the surface during the mainshock; the waveforms were asymmetric in shape and had different amplitudes for the down-going and up-going motions for a small duration (see the next section). The shift of peak frequency and relatively larger DNL value are indicative of a nonlinear site response at the site IBUH01. However, the evaluation of nonlinear site response at the site IBUH01 based on spectral ratios may not be suitable due to the presence of asymmetric waves on the surface recordings (e.g., Aoi et al. 2008), and hence, the results presented above are only for information. Similarly, the site HDKH01 (Fig. 7c) showed a possibility of nonlinear site response during the mainshock. The vertical PGA at the surface was approximately 317 cm/s^2. The peak frequency was shifted toward lower one (from about 18–6 Hz) with larger amplification than that in the weak-motions. The DNL value was 3.8. At the site IBUH06 (Fig. 7h), the DNL value was 5, and a systematic decrease in spectral ratios was found at frequencies larger than about 10 Hz. This latter feature was not clear at the other sites. These results may indicate that the vertical component at IBUH06 experienced a small degree of nonlinear site response during the mainshock. Also, the site IBUH07 (Fig. 7i) may have experienced a small degree of nonlinearity as suggested by the small shift of the first peak frequency and the substantial decrease in spectral ratios at about 3–6 Hz. The DNL value for the site was 4.1. In fact, two comparable peaks can be seen in the spectral ratios at the IBUH07 site during the strong-motions at 2.1 and 12.3 Hz approximately. If the peak at higher frequency is neglected considering the range of scattering for weak-motions, a systematic decrease in spectral ratios between about 2- and 10-Hz points toward a nonlinear site response. Except for the four sites mentioned above, the other sites did not show clear signatures of nonlinearities in vertical component ground motions; the DNL values at the sites were between 2.2 and 3.3 (see also Table 2).

The peak frequencies between S-to-B spectral ratios for horizontal components (H-to-H) (x axis) and vertical components (V-to-V) (y axis) during weak-motions are plotted in Fig. 8a. It can be seen in the figure that the peak frequencies are systematically higher for the V-to-V spectral ratios than those for the H-to-H spectral ratios except at one site, indicating that the two spectral ratios may represent the results for two different wave types:

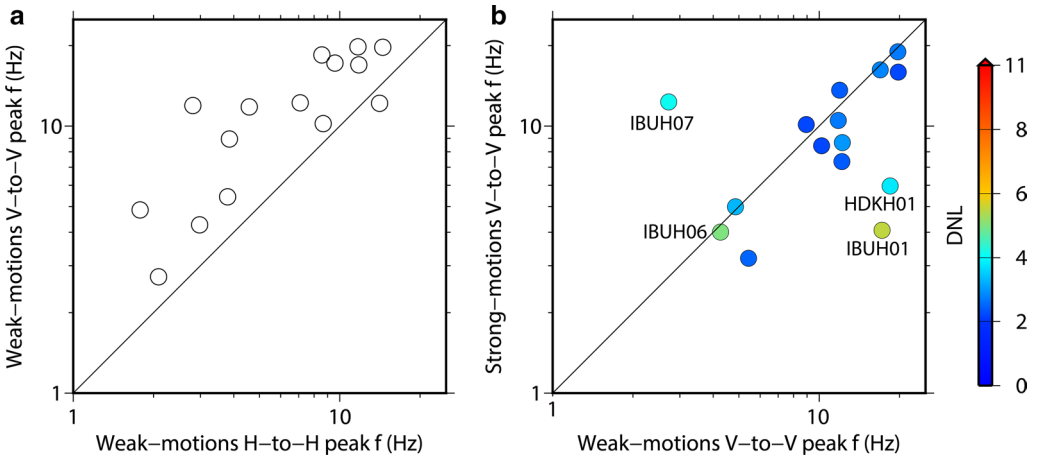

Fig. 8 **a** Comparison of peak frequencies between surface-to-borehole spectral ratios for horizontal components (H-to-H) (x axis) and vertical components (V-to-V) (y axis) during weak-motions. **b** Comparison of peak frequencies between surface-to-borehole spectral ratios for vertical components (V-to-V) during weak-motions (x axis) and strong-motions (y axis). The data points are color-coded by DNL values computed based on vertical component spectral ratios (V-to-V). Some data points that deviate largely from the diagonal line in **b** are provided with their site codes close to the data points

horizontal components mostly for S-waves and vertical components mostly for P-waves, at least for higher-frequency components. In the case of mainshock, the late-arriving P-waves might have also contaminated the S-waves in the vertical components and contributed to the higher predominant frequency. The peak frequencies for the V-to-V spectral ratios for the mainshock and weak-motions are plotted in Fig. 8b. They are similar at most sites. At two sites, namely IBUH01 and HDKH01 having relatively larger DNL values (the two data points near lower right corners in Fig. 8b), the peak frequencies during strong-motions are smaller than those for the weak-motions. However, a reverse trend for peak frequency can be seen at one site near 2.7 Hz along the horizontal axis; this is at the IBUH07 site due to the reason briefly mentioned in the previous paragraph. The spectral ratios at the site IBUH07 had two comparable peaks at about 2.1 and 12.3 Hz during strong-motions. The peak at 12.3 Hz was slightly larger than the peak at 2.1 Hz (see Fig. 7i). Therefore, the plot for IBUH07 is a purely mathematical one in Fig. 8b.

Here we discuss the possible mechanisms qualitatively for the nonlinear site response on the vertical components. Sato and Kanatani (2006) suggested that the nonlinear site response can occur on the vertical motions (pressure waves) for unsaturated soils because the change of bulk modulus and damping for P-waves occur in response to strong input motions in addition to the changes in shear modulus and damping for S-waves. Meanwhile, they pointed out that the effect of change of shear modulus and damping for S-waves do not contribute significantly to induce nonlinear site response on the vertical motions for the saturated soil. Between the three sites, namely HDKH01, IBUH06, and IBUH07 which are suspected for nonlinear site response on the vertical components, available PS-logging data suggest that the sites HDKH01 and IBUH06 might be unsaturated in its top layers during the earthquake. At the site HDKH01, the measured P- and S-wave velocity in the top 4 m of soil is 860 and 120 m/s, respectively; the layer beneath the above layer has a thickness of 4 m and has P- and S-wave velocity of 1200 and 360 m/s, respectively. The recorded PGAs on the horizontal and vertical components were approximately 663 and 317 cm/s^2, respectively, at the HDKH01 site (see Table 2). Indeed, the site experienced a significant nonlinear site response on the horizontal components as discussed in the previous section, which means that the nonlinear site response on the vertical component at the HDKH01 site is likely to be due to the changes in P-wave velocity and damping for the P-waves in addition to the corresponding changes for S-waves. At the site IBUH06, the top 5 m of soil has P- and S-wave velocity of 460 and 200 m/s, respectively; the second layer having a thickness of 5 m has P- and S-wave velocity of 850 and 340 m/s, respectively. The recorded PGAs on the horizontal and vertical components were approximately 260 and 203 cm/s^2, respectively, at the IBUH06 site (see Table 2). The site also experienced nonlinear site response on the horizontal components (Fig. 5h). The smaller P-wave velocity and relatively large PGA on the vertical component suggest that the changes in both the P- and S-wave velocities and corresponding damping in response to strong input motions might have induced nonlinear site response on the vertical motions at the site IBUH06. At the site IBUH07, the P-wave velocity in the top 5 m and next 8 m of soil is 1600 m/s; the S-wave velocities in the layers are 400 and 200 m/s, respectively (velocity inversion is noted). The recorded PGAs on the horizontal and vertical components were approximately 222 and 82 cm/s^2, respectively (see Table 2). The PS-logging velocity model and PGAs suggest that the change in P-wave velocity and damping for it may not be significant at the site, and the site might have experienced nonlinear site response on the vertical motions due to the changes in S-wave velocity and damping for S-wave. We defer the quantitative evaluation of nonlinear site response at the sites to future study.

Direct evidence of nonlinear site response on vertical components

In this section, we present the direct evidence that we think of nonlinear site response on vertical component waveforms at two sites (IBUH01 and HKD127) during the mainshock. See Fig. 3 for site location. The surface and borehole vertical component recordings at the sites are plotted in Fig. 9. The surface acceleration waveforms at both the IBUH01 and HKD127 showed some characteristic pulses barely reported in strong-motions: the larger amplitude of up-going acceleration pulses (often exceeding 1 g) than that for down-going ones (often lower than 1 g) and duration of up-going acceleration pulses smaller than that of the down-going ones. The borehole recordings at the site IBUH01 did not show the features above. The largest peak ground accelerations of up-going and down-going pulses at IBUH01 were approximately 1060 and -745 cm/s^2, respectively, at the surface, while the corresponding values at a depth of 101 m were approximately 75 and -84 cm/s^2, respectively. Similarly, the largest PGAs of up-going and down-going pulses at HKD127 were approximately 1590 and -880 cm/s^2, respectively. The ratio of the sums of duration for up-going and down-going pulses for a time window of 4 s plotted in Fig. 9b is 1.15 at IBUH01 and 1.07 at HKD127. The ratios become approximately 1.3 and 1.6 at the former and latter sites when the ratios are computed from the pertinent pulses

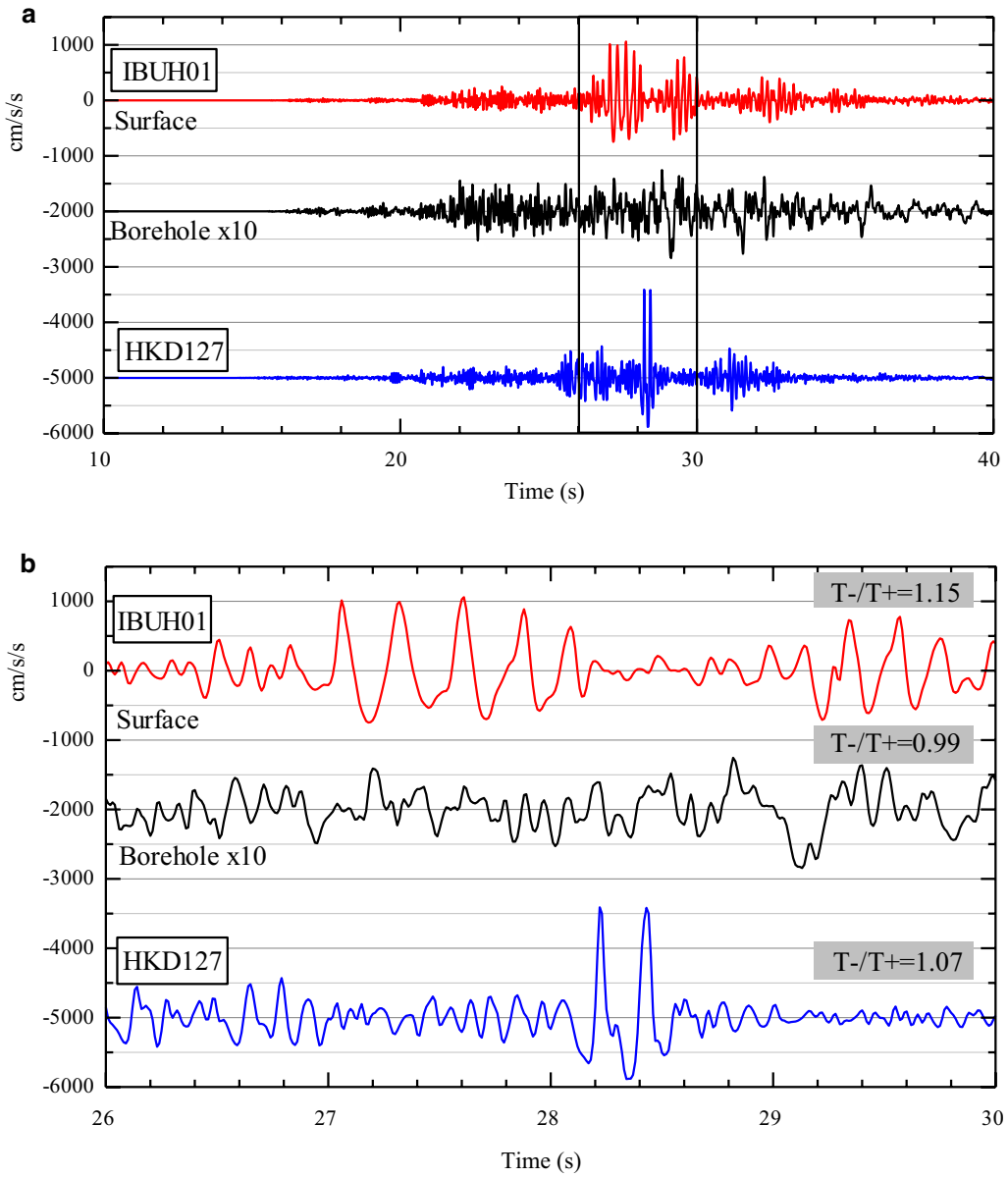

Fig. 9 **a** Vertical component acceleration recordings at the surface (upper panel) and borehole (middle panel) at site IBUH01 and the surface at HKD127 (lower panel). The values for the borehole recordings are magnified by a factor of 10 to aid visual comparison. A black rectangle denotes the portion of the plot, which is enlarged in **b**. The ratio of total duration of negative pulses to the total duration of positive pulses is indicated above each trace for the time window from 26 to 30 s in **b**. See Fig. 3 for site location and text for further explanation

only. These observations were similar to those observed during the 2008 Mw 6.8 Iwate-Miyagi crustal earthquake, Japan (Aoi et al. 2008). The asymmetric pulses were pertinent for longer durations at IWTH25 during the Iwate-Miyagi earthquake than those during the present earthquake. Yamada et al. (2009) summarized the characteristics of asymmetric waveforms in amplitude and duration on vertical component ground motions that had been recorded prior to the largest known vertical acceleration (Aoi et al. 2008), including the features at the site IWTH25 during the Iwate-Miyagi crustal earthquake.

The mechanisms, threshold motions, site geology, etc. to induce large amplitude asymmetric vertical ground motions are not well understood. Interested readers can find an intuitive explanation for asymmetric waves in extreme vertical component accelerations in Aoi et al. (2008), who explained the phenomena by trampoline

effect. Some other explanations on mechanisms for the asymmetric waves can be found in Yamada et al. (2009), who explained the asymmetric waves as slap down phases. Tobita et al. (2010), based on numerical analysis, concluded that the asymmetrical waveforms might be related to the different behaviors of soils in compression and tension.

The S-to-B spectral ratios of vertical components at IBUH01 for the mainshock, weak-motions, and an aftershock that occurred about 3 h later close to the mainshock hypocenter are plotted in Fig. 10 for the site IBUH01. The aftershock recordings at the surface had a horizontal vector PGA of approximately 124 cm/s^2 and vertical PGA of approximately 51 cm/s^2. In Fig. 10, it can be seen that the peak frequency of spectral ratios from the aftershock is more similar to that from the weak-motions than that from the mainshock recordings. The asymmetrical waveforms also were not present on the aftershock recordings. Thus, it is likely that the characteristic asymmetric waves for the down-going and up-going accelerations, which were recorded during the mainshock only, were due to the nonlinear soil response at the sites during the mainshock.

Here we explain the shallow soil velocity profiles briefly at the two sites mentioned above. The P- and S-wave velocity profiles based on PS-loggings are shown in Fig. 11. The velocity model based on PS-logging is available down to the depth of 10 m at the HKD127 site, while the model reaches to a depth of 101 m at the site IBUH01. Since the two sites are closely located, the deeper subsurface model beneath the sites may be considered similar. Based on the PS-logging data, the average S-wave velocities in the upper 10 m of the soil column beneath the sites IBUH01 and HKD127 are approximately 183 and 189 m/s, respectively. On the other hand, the P-wave velocities in the upper 10 m beneath the two sites are approximately 571 and 982 m/s, respectively. The maximum amplitude of the up-going pulses was relatively larger at the site HKD127 than that at the IBUH01 site. The maximum and minimum PGAs at the site IWTH25 were 3866 and 1703 cm/s^2, respectively. We examined the PS-logging data at the site IWTH25 and found that the shallow soil layers are stiffer than those at the sites HKD127 and IBUH01; the average S-wave and P-wave velocities in the upper 10 m of the soil column beneath the site IWTH25 were approximately 465 and 1073 m/s, respectively. Yamada et al. (2009) noted that the sites that showed asymmetric waves were relatively stiff sites. These observations may suggest that the local site geology is one of the important factors to understand the mechanisms of asymmetric waves observed on vertical component recordings during strong-motions, and stiff sites may lead to stronger asymmetrical pulses with large

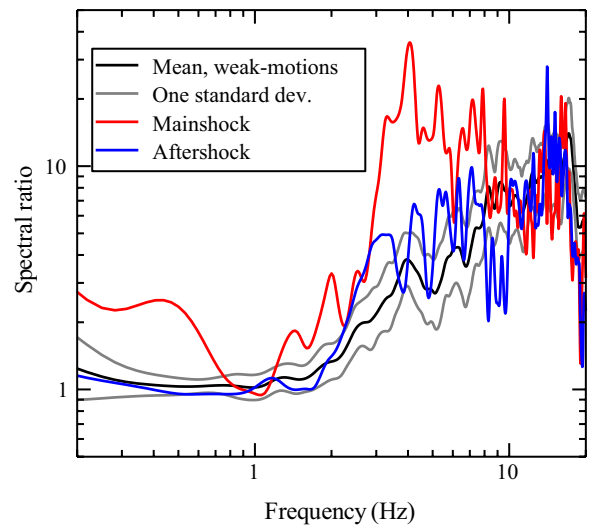

Fig. 10 Comparison of surface-to-borehole spectral ratios of vertical component acceleration recordings (V-to-V) at site IBUH01 during weak-motions (mean of the weak-motions, black line), mainshock (red line), and an aftershock (blue line). The gray lines denote the range of plus–minus one standard deviation from the mean of weak-motion spectral ratios. The aftershock (Mj = 5.4, focal depth = 40 km, epicentral distance = 24.3 km, back azimuth = 142.6°) occurred on September 6, 2018, at 06:11 JST, about 3 h later than the mainshock

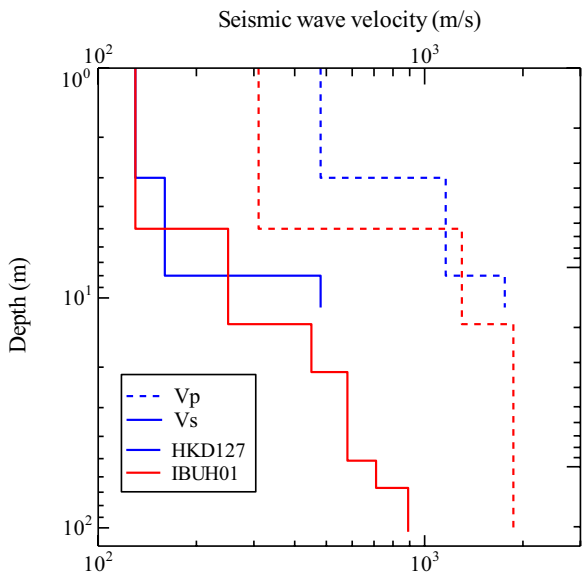

Fig. 11 P- and S-wave velocity profiles based on PS-loggings at sites IBUH01 (red lines) and HKD127 (blue lines). The P- and S-wave velocity profiles are drawn in dashed and solid lines, respectively. The vertical axis is drawn in log-scale to show the shallow layers clearly. The scale begins from 1 and corresponds to the free surface at the recording station

vertical accelerations during strong-motions. We explore the characteristics of nonlinear site response using the single-station H-to-V spectral ratio technique at selected sites of the KiK-net and K-NET in the next section.

H-to-V spectral ratios at surface KiK-net and K-NET sites

In this paper, we obtained the H-to-V spectral ratios of surface recordings at the KiK-net and K-NET sites depicted in Fig. 3. The spectral ratios were obtained as the vector sum of two horizontal components Fourier spectral amplitudes divided by the corresponding Fourier spectral amplitudes of the vertical component. The H-to-V spectral ratios for the weak- and strong-motions at the KiK-net sites are plotted in Fig. 12 along with the S-to-B spectral ratios for horizontal components during the mainshock. The sites are arranged in the same order as that in Figs. 5 and 7. Figure 12 shows that the two types of mean spectral ratios for the weak-motions (H-to-V: black lines, and S-to-B: blue lines) are generally different. In the same way, the corresponding ratios during the mainshock (H-to-V: red lines, and S-to-B: green lines) are also different. These results are generally expected as the S-to-B spectral ratios are dependent on both site geology and depth of the down-hole sensor (e.g., Steidl et al. 1996) while the H-to-V

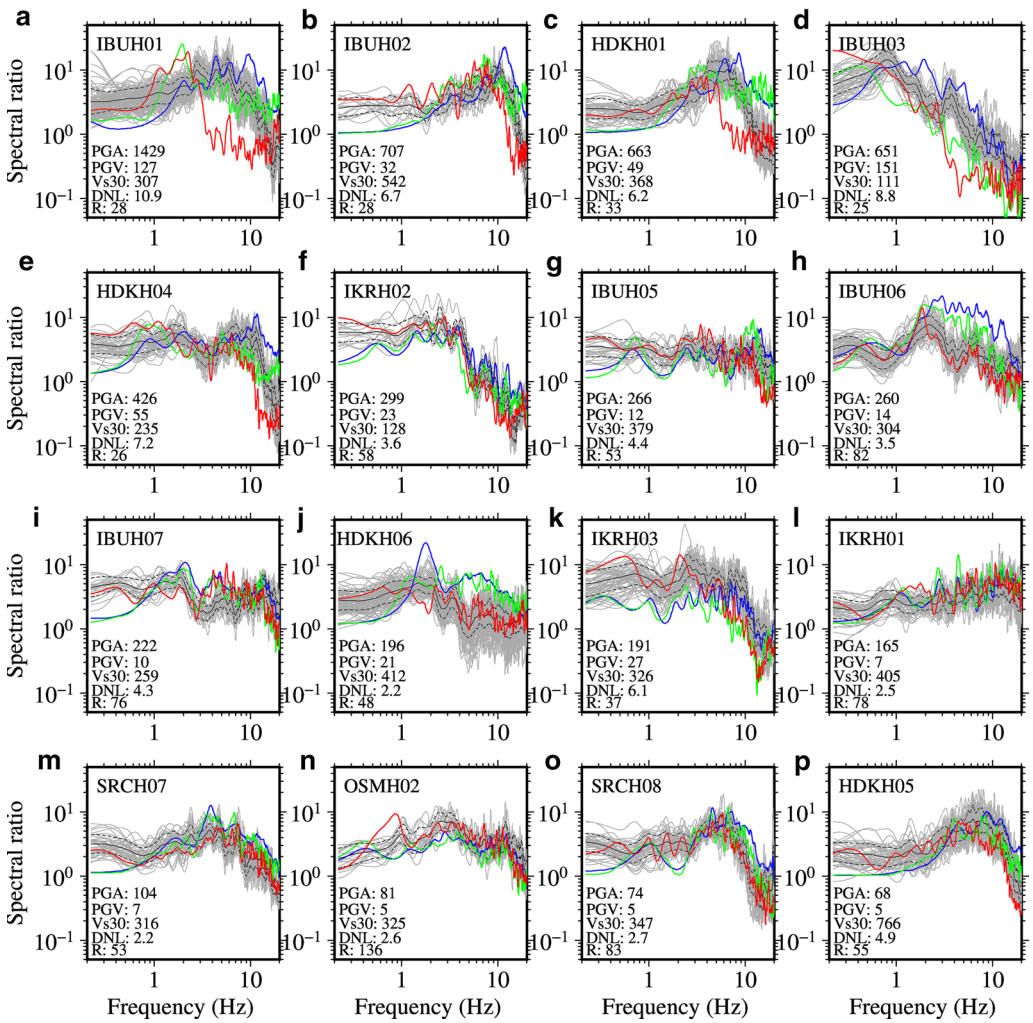

Fig. 12 Plots of H-to-V spectral ratios of surface recordings during weak-motions (gray lines) and those during the mainshock (red lines) at KiK-net sites. The green and blue lines denote the S-to-B spectral ratios of horizontal components (H-to-H) for mainshock and weak-motions, respectively (see also Fig. 5). The plots are arranged in order of the sites depicted in Figs. 5 and 7. Solid black lines denote mean spectral ratios for weak-motions and dashed gray lines denote one standard deviation. The horizontal vector PGA in units of cm/s^2, horizontal vector PGV in units of cm/s, Vs30 in units of m/s, DNL values, and fault-to-site distance (R) in units of km are also included for each site. See Fig. 3 for site location

spectral ratios are mainly controlled by the site geology (e.g., Kawase et al. 2011).

The peak frequencies for the two types of spectral ratios for weak-motions are plotted in Fig. 13a. It can be seen that the peak frequencies are comparable except at few sites, where the peak frequencies are higher for S-to-B spectral ratios. The site IBUH05 is exceptional; the weak-motions S-to-B spectral ratios had peak at frequency ~ 14.5 Hz while the weak-motions H-to-V had peak at frequency ~ 2.7 Hz. The S-to-B spectral ratios during the strong-motions suggested nonlinear site response, and the reasonable shift of peak frequency was recognized (from ~ 14.5 to 12 Hz) (see Fig. 5g). The H-to-V spectral ratios during the strong-motions also indicated a small degree of nonlinear site response, and the spectral ratios were smaller in relation to weak-motions at frequencies larger than about 10 Hz, but the shift of peak frequency was not evident (see Fig. 12g). The lack of clear peak for H-to-V spectral ratios for the weak-motions as well as the strong-motions may be one of the possible reasons for the large discrepancy of the peak frequencies between the two types of spectral ratios at the site IBUH05. The DNL values for the mainshock based on the two types of spectral ratios are plotted in Fig. 13b, and they may be considered similar considering the reasonable scattering of the spectral ratios. Similarly, the peak frequencies for the two types of spectral ratios during the mainshock are comparable at most sites as shown in Fig. 13c. Here, we note that the larger DNL value at the site IBUH01 based on the H-to-V spectral ratios is partially due to the effect of nonlinear amplification on the vertical component recording at the surface (see Fig. 7a). The above result suggests that the H-to-V spectral ratio method may not be suitable to reliably extract the degree of change in site response such as the reduction in spectral amplification factors at higher frequencies if the vertical components experienced nonlinear site response. However, as evident in Fig. 13b, c, the data points that deviate largely from equality are not systematic between the S-to-B and H-to-V methods for strong-motions. The H-to-V spectral ratio method is still able to detect the nonlinear site response in similar ways to that of S-to-B spectral ratio method of horizontal components, which was primarily due to the different ranges of frequencies that were affected on the horizontal and vertical component ground motions. The horizontal motions were affected up to relatively lower frequencies than those for vertical motions by the nonlinear site response (for example, see Figs. 5a, c, h and 7a, c, h for sites IBUH01, HDKH01, and IBUH06, respectively).

Here we discuss the nonlinear site response at the K-NET sites. The H-to-V spectral ratios at the selected 16 sites of K-NET are plotted in Fig. 14. All the sites recorded horizontal vector PGA of 200 cm/s^2 or larger. The peak ground motions for the mainshock, predominant frequencies during the mainshock and weak-motions, and the DNL values at the K-NET sites are provided in Table 3. The sites, namely HKD127, HKD125, HKD128, HKD103, HKD126, HKD124, HKD129, HKD105, HKD184, HKD131 (Fig. 14a, b, c, d, e, f, h, i, j, l), showed the shift of predominant frequencies and reduction in higher-frequency spectral ratios in different amounts, suggesting that the sites experienced various degrees of nonlinear site response. The horizontal vector PGAs were between 387 cm/s^2 and 1318 cm/s^2, and the DNL values ranged between 3.3 (HKD125, Fig. 14b) and 13.4

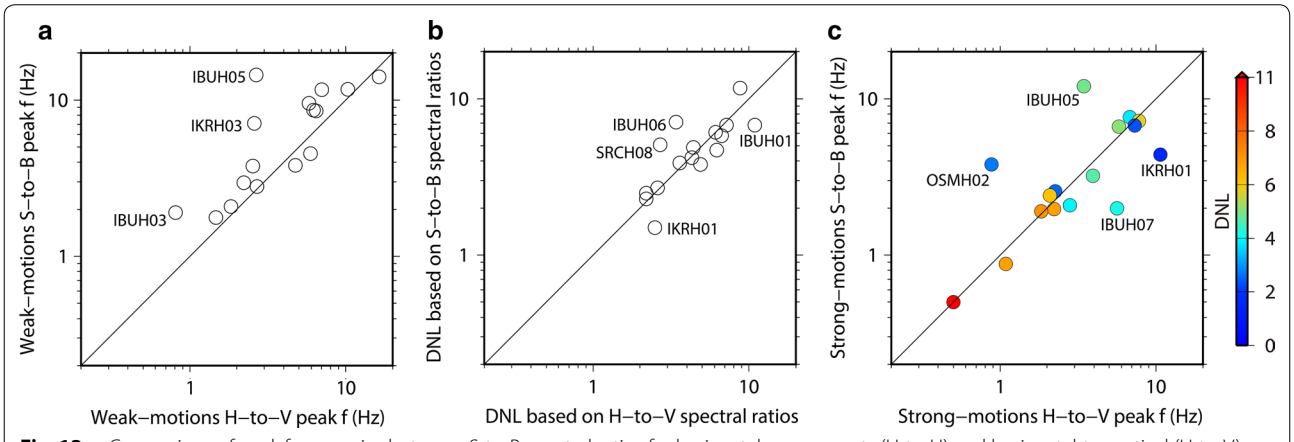

Fig. 13 **a** Comparison of peak frequencies between S-to-B spectral ratios for horizontal components (H-to-H) and horizontal-to-vertical (H-to-V) spectral ratios at the surface for weak-motions. **b** Comparison of DNL values based on S-to-B spectral ratios for horizontal components (H-to-H) and H-to-V spectral ratios at the surface. **c** Comparison of peak frequencies between S-to-B spectral ratios for horizontal components (H-to-H) and H-to-V spectral ratios at the surface for strong-motions. The data points are color-coded by DNL values based on the S-to-B spectral ratios. Some data points that deviate largely from the diagonal lines are provided with their site codes near the data points

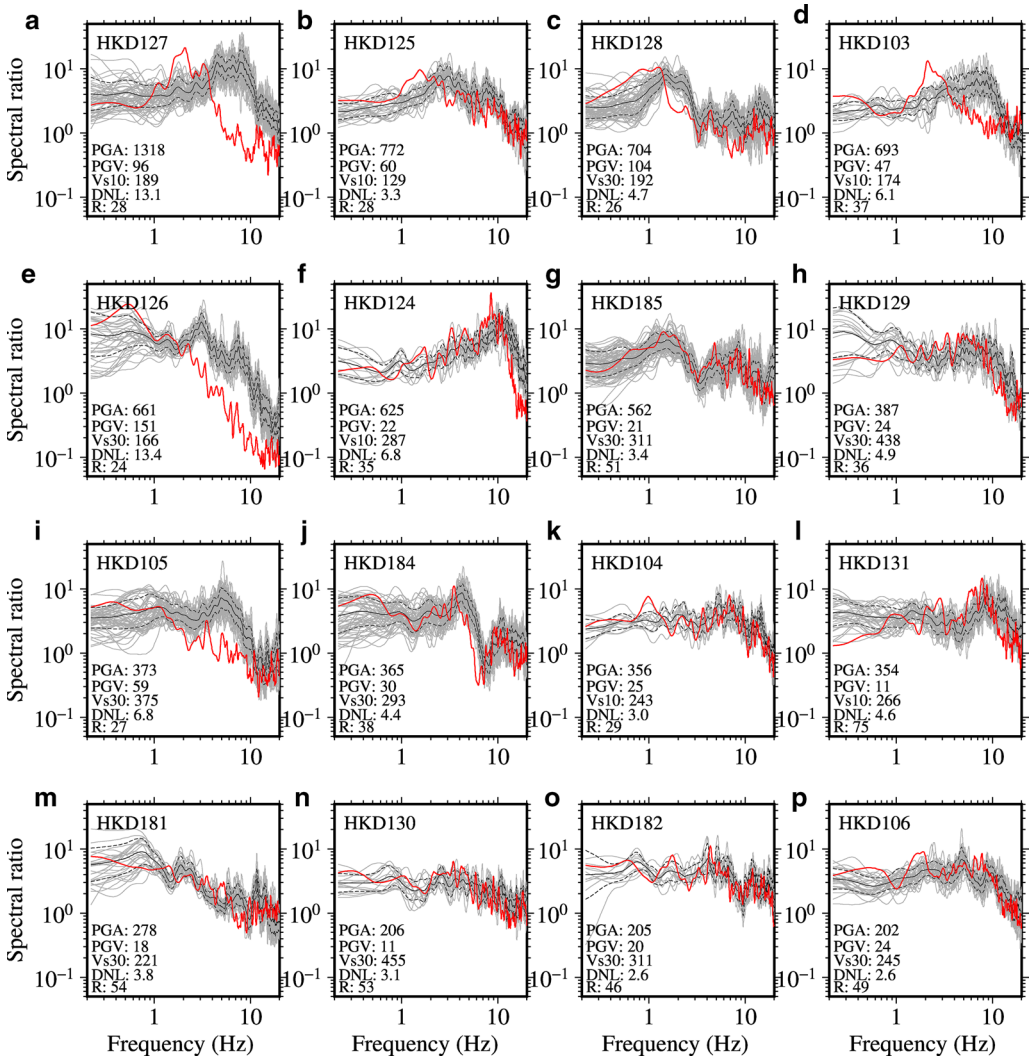

Fig. 14 Plots of H-to-V spectral ratios of surface recordings during weak-motions (gray lines) and those during the mainshock (red lines) at K-NET sites. See Fig. 3 for site location. The plots are arranged in order of decreasing horizontal vector PGAs in panels **a**–**p**, respectively. Solid black line denotes mean spectral ratios for weak-motions, and dashed gray lines denote one standard deviation. The horizontal vector PGA in units of cm/s^2, horizontal vector PGV in units of cm/s, Vs30 in units of m/s, DNL values, and fault-to-site distance (*R*) in units of km are also included for each site

(HKD126, Fig. 14e) at the sites. The site HKD126 with maximum DNL value of 13.4 showed a marked reduction in spectral ratios at frequencies higher than about 2 Hz during the mainshock, and the shift of predominant frequency was from 3.06 Hz to 0.53 Hz. The DNL value at the site HKD127 (Fig. 14a) was 13.1, and the shift of predominant frequency was from 7.78 to 2.06 Hz. As the site HKD127 experienced nonlinear site response on the vertical component as discussed in the previous section, the DNL value based on H-to-V spectral ratios may not be suitable to infer the degree of nonlinearity at the site. However, by analogy with the site IBUH01, the information on the shift of predominant frequency is useful for the identification of soil nonlinearity. The other six sites, namely HKD185, HKD104, HKD181, HKD130, HKD182, HKD106 (Fig. 14g, k, m–p), had DNL values between 2.6 (HKD182 and HKD106) and 3.8 (HKD182), and the sites did not show clear shift of predominant frequencies except an apparent shift of frequencies between about 1 and 10 Hz at the site HKD182. The horizontal vector PGAs ranged between 206 and 356 cm/s^2 at the sites except at HKD185 that recorded 562 cm/s^2. Despite the large PGA, the DNL value at HKD185 was 3.4. The spectral ratios as well as the DNL values at the sites HKD105 and HKD184 (Fig. 14i, j), for example where the PGAs were smaller than those at the site HKD185, indicated

the nonlinear site response at the sites. Accordingly, the nonlinear site response is not related by simple relation with the PGAs at the surface, and rather, it signifies that the nonlinear site response is primarily controlled by soil stiffness and input ground motions at the bottom of the soil layers discussed briefly in the next section.

The peak frequencies of S-to-B spectral ratios of horizontal components during strong-motions (mainshock) and weak-motions at the KiK-net sites and those of H-to-V spectral ratios at K-NET sites are plotted in Fig. 15. It is evident in the figure that the peak frequencies of the spectral ratios for the mainshock are mostly lower than those for the weak-motions except at a site (HKD129). The weak-motion spectral ratios at the HKD129 site are comparable to the spectral ratios during the mainshock at frequencies between about 0.5 and 10 Hz, and the ratios are almost flat between those frequencies as shown in Fig. 14h. Therefore, the difference between the weak-motion and strong-motion peak frequencies at the HKD129 site is mainly due to similar spectral ratios. Figure 15 suggests that the larger DNL values are related to larger PGAs and lower Vs30 values. However, the Vs30 values do not always indicate the plausibility of nonlinear site response sufficiently as discussed briefly in the next paragraph.

Among the sites analyzed in this study, two KiK-net sites, namely IBUH02 and HDKH05, have Vs30 values exceeding 500 m/s (see Table 2). The IBUH02 site clearly showed signatures of nonlinear site response (see Fig. 5b); the Vs30 value at the site is 542 m/s, and horizontal vector PGA was 707 cm/s^2. A site with such high Vs30 value is generally expected to undergo linear site amplification. However, a close examination of the PS-logging data at the site showed that the Vs30 is 130 m/s for the top 2 m of soil layer and 280 m/s for the next 5 m, which overlies the stiffer layers having Vs value of 810 m/s and larger. The above findings may suggest that the top layers having smaller Vs values overlying the more competent large impedance layers may experience significant nonlinear site response, and hence, the Vs30 values may not be a good indicator for nonlinear site response in every case. The HDKH05 site showed a small degree of nonlinear site response (see Fig. 5p) despite smaller input motions (the horizontal vector PGA was approximately 68 cm/s^2 at the surface and 26 cm/s^2 at a depth of 100 m) and large Vs30 value of 766 m/s. A close examination of the PS-logging data at the site showed that the Vs30 is 250 m/s for the top 2 m of soil layer, 470 m/s for the next 4 m, and larger than 1000 m/s for the underlying layers. These velocity models together with the above observations corroborate that the layers having S-wave velocities smaller than about 300 m/s are strongly susceptible to nonlinear site response during strong-motions.

An ad hoc equation for nonlinear site amplification

We found that the most sites at fault distances shorter than about 50 km experienced nonlinear site response during the mainshock, and it was confirmed that the sites gained the motions in the frequency bands that corresponded to the enhancement of amplification due to

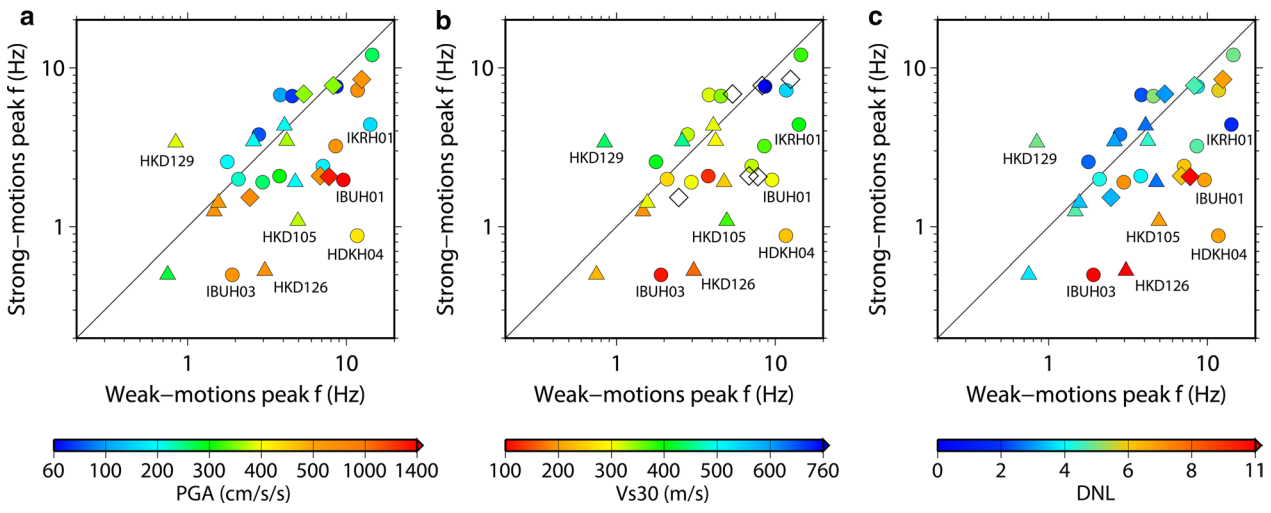

Fig. 15 Comparison of peak frequencies from strong-motions (mainshock) and weak-motions S-to-B spectral ratios for horizontal components at the KiK-net sites (circles) and H-to-V spectral ratios at the K-NET sites (triangles). The data points are color-coded by horizontal vector PGAs at the surface in **a**, Vs30 values in **b**, and DNL values based on the S-to-B spectral ratios in **c**, respectively. The sites where Vs30 values were not estimated are denoted by diamonds (see Table 3 for the Vs10 values at the sites). Some data points that might be of interest to readers are provided with their site codes near the data points

nonlinear site response. Even though both the PGA and PGV are affected by nonlinear site response, it is mostly the PGV that is amplified because the relatively longer-period ground motions get enhanced due to nonlinear site response. Kamiyama (1992) obtained a nonlinear site amplification model at a site statistically as a function of maximum particle velocity at a virtual rock site. Abrahamson and Silva (1997) obtained nonlinear site amplification terms in their GMPE as a function of rock site PGA. More recent studies (e.g., Walling et al. 2008; Kamai et al. 2014) proposed the rock site PGA as one of the input motion parameters as well as the Vs30 to address the unequal nonlinear site response at different site conditions. The studies mentioned above indicate that the strength of input motions at the base of a soil site may be represented in terms of the corresponding PGA or PGV for a virtual rock site at the site of interest. In this study, we followed the recent trend of using PGA as a reference motion to incorporate nonlinear site response in GMPEs. Over the last 40–50 years, an enormous amount of literature has been accumulated in the numerical simulation of nonlinear site response. For an overview of quantification of nonlinear site response by numerical simulations, we refer the paper by Régnier et al. (2016) and the references therein.

Here we derived a correction formula for the PGVs with reference to the median values obtained from GMPEs. We first obtained the rock site PGAs at the selected sites using the GMPE by Si and Midorikawa (1999). These PGAs and Vs30 values at the sites were treated as independent variables, and the residuals for PGVs plotted in Fig. 2d were fitted against the two variables. Finally, we obtained the following relation (Eq. 3) between PGV residuals, input PGAs (rock site PGAs ≥ 50 cm/s^2), and Vs30 values (between 110 and 540 m/s approximately) by linear regression:

$$\log_{10}\left(\frac{\text{obsPGV}}{\text{prePGV}}\right) = 0.0399 + 0.0028\text{PGA}_{\text{rock}} - 0.0002\text{Vs}_{30} \tag{3}$$

where obsPGV is the observed PGV (larger of two components), prePGV is the predicted PGV taking account of Vs30 in GMPE by Si and Midorikawa (1999), PGA_{rock} is the predicted PGA at a virtual rock site at the distance of site of interest using the GMPE for PGA in Si and Midorikawa (1999). To confine the equation within the range of nonlinear response, we obtained the equation using the data points at which the DNL values were 4 or larger at the both K-NET and KiK-net sites. This resulted in the rock site PGAs ≥ 50 cm/s^2 and Vs30 values smaller than about 540 m/s in the above analysis. The standard deviation of the residuals for Eq. 3 is 0.1304 in base-10 log-scale. The obtained coefficients for PGA and Vs30 are generally in good agreement with the expected results that the PGV should decrease with the increase in Vs30 values and should increase with the increase in input

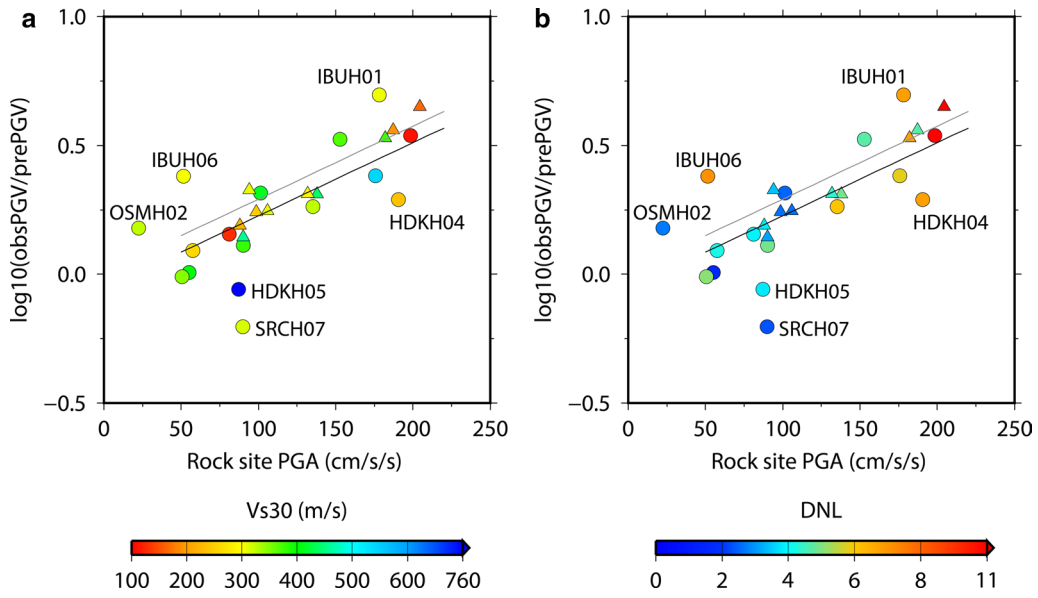

Fig. 16 Plots of logarithmic residuals for PGVs as a function of rock site PGAs using the GMPEs in Si and Midorikawa (1999). The data are color-coded by Vs30 values in **a** and DNL values in **b**, respectively. The KiK-net and K-NET sites are indicated by circles and triangles, respectively. The gray and solid lines denote the correction values for PGVs as a function of PGAs at rock sites using Eq. 3 for Vs30 values of 150 and 450 m/s, respectively. Note that the data points having DNL values smaller than 4 were excluded in the derivation of Eq. 3; they are included in the above plots for reference only. Some data points are provided with their site codes for reference close to the data points

motions. The PGV residuals are plotted against rock site PGAs in Fig. 16; a linear relationship can be easily seen between the two variables. The data points are color-coded by Vs30 and DNL values. The lines representing the correction values for PGVs in base-10 log-scale are also plotted in the figure for Vs30 values of 150 m/s (gray line) and 450 m/s (black line). It can be seen that the main contributor to the correction value is the input PGA, and this finding is similar to the previous results (e.g., Campbell and Bozorgnia 2008, 2014). The PGVs plotted in Fig. 2b were corrected by Eq. 3 at sites where input PGAs ≥ 50 cm/s^2 were calculated, and these new values are plotted in Fig. 17. It can be seen that the same GMPE describes the data well after the corrections for the nonlinear site response.

Since Eq. 3 is derived for a specific data set for a single event and limited site conditions, we consider the correction coefficients an ad hoc result. We continue to investigate the relationships for other events as an effort toward our long-term goal of accomplishing the reliable prediction of ground motions for seismic hazard analysis and earthquake early warnings in our future studies.

Discussions and conclusions

We analyzed the strong-motion data of the 2018 Mw 6.6 Hokkaido eastern Iburi earthquake to understand the peak ground motions and characteristics of nonlinear site response during the earthquake. We compared the observed PGAs and PGVs with the values from the GMPEs by Si and Midorikawa (1999), which have been widely used for seismic hazard evaluation in Japan. We found that the data at fault distances larger than about 50 km were generally explained by the ground motion prediction equations very well. In contrast, in the regions of high seismic intensity at smaller distances and soft sites, the equations underestimated the data substantially. The underestimation was more evident to PGVs.

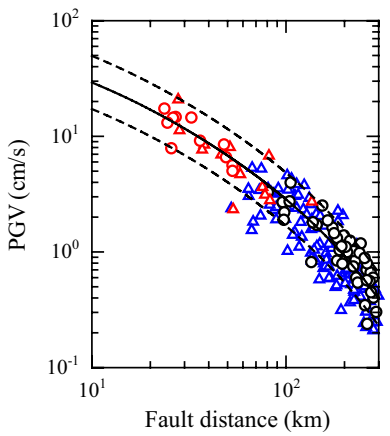

Fig. 17 Observed PGVs after corrections for nonlinear site effects plotted as a function of fault distance. The values were adjusted for nonlinear site effects if rock site PGAs exceeded 50 cm/s^2, and Vs30 values were lower than about 550 m/s. For further explanation, see the text and figure captions in Fig. 2

We computed and analyzed the S-to-B spectral ratios of horizontal components, S-to-B spectral ratios of vertical components, and H-to-V spectral ratios of surface recordings for the mainshock and weak-motions at 16 KiK-net sites. Only the H-to-V spectral ratios were analyzed at the equal number of K-NET sites because the K-NET sites consisted of sensors only at the surface. We obtained DNL values following the method of Noguchi and Sasatani (2008) using the spectral ratios between 0.5 and 20 Hz. The threshold DNL value of 4 for H-to-V spectral ratio method and 2.5 for S-to-B spectral ratios of horizontal components as suggested by Noguchi and Sasatani (2011) generally served as a good criterion to identify nonlinear site response in this study. Furthermore, in the present study, we found that a DNL value of 3.5 or larger may indicate a nonlinear site response based on the S-to-B spectral ratios of vertical components for the time window that corresponds to S-waves on horizontal components.

By comparing the weak-motions and strong-motions (mainshock) spectral ratios, we found that the sites having relatively smaller Vs30 values in regions of stronger input motions experienced a larger degree of nonlinear site response. These results were consistent with previous results regarding the commonly reported conditions for nonlinear site response. We found that a few sites might have experienced nonlinear site response on horizontal components having PGAs as low as about 70 cm/s^2 depending on the site condition. In the earlier literature and the engineering community in general (e.g., Kramer 1996, p. 318), a decrease in PGAs at soil sites during strong-motions in comparison with weak-motions has been well accepted. More recent studies supported by many data (e.g., Campbell and Bozorgnia 2008, 2014) have emphasized the nonlinear amplification of ground motions at wide frequencies that depends on the input PGAs. We found that, during the 2018 Mw 6.6 Hokkaido eastern Iburi earthquake, the nonlinear amplification was larger by one order of magnitude at the IBUH01 site, and at the other several sites which experienced large intensities (e.g., IBUH03, HDKH01, HDKH04, HKD126, HKD128), the increase in amplification at lower frequencies in relation to the linear case was substantial. Indeed, amplifications decreased during strong-motions at the predominant frequencies of the linear case at the sites mentioned above, and at the site IBUH03, the horizontal vector PGA at the surface was somewhat smaller than that at the borehole at a depth of 153 m (651 cm/s^2 vs

795 cm/s^2 approximately). Contrarily, the horizontal vector PGV was significantly amplified at the site IBUH03 (surface 151 cm/s vs borehole 39 cm/s). We think that the nonlinear amplification was one of the main causes of high JMA intensities and underestimation of the observed PGVs at smaller fault distances. These observations suggest for greater attention to nonlinear site response in seismic hazard analyses.

It is noteworthy to mention here that the sites IBUH01 and HKD127 experienced nonlinear site response on both the horizontal and vertical component ground motions at the surface. It is still not all out about the threshold motions and mechanisms that cause the generation of large amplitude asymmetric pulses, but the relatively stiffer site condition appears to be one of the factors in addition to the large vertical input motions at the base rock. Our analyses based on the S-to-B spectral ratios of vertical components suggested that most sites that showed nonlinear site response on horizontal components did not show nonlinear site response on vertical components. These findings suggested that the H-to-V spectral ratio method is equally useful as the S-to-B spectral ratio method to identify nonlinear site response at least in a statistical sense. However, we note that some sites might have experienced nonlinear site response on vertical components for vertical PGAs as low as approximately 80–200 cm/s^2. This means that the DNL values obtained from the H-to-V method are not reliable if the site experienced nonlinear site response on vertical components. Larger DNL values as obtained in this study imply the larger reduction in higher-frequency components. Therefore, caution should be maintained to estimate the spectral amplifications at higher frequencies during strong-motions based on the H-to-V spectral ratio method. Interestingly, the shift of predominant frequency to lower one was quite similar between the S-to-B and H-to-V spectral ratio methods even at a site that experienced nonlinear site response on the vertical component. In our analysis, this was because the horizontal motions were affected up to lower frequencies than those for vertical motions by the nonlinear site response.

By considering the PGAs at virtual rock sites as reference input motions, we obtained an ad hoc equation to account for nonlinear site amplification for PGVs with reference to the GMPEs in Si and Midorikawa (1999). We found that the input motions largely control the deviations from the median predictions given the identical site conditions. For a given input motion, the larger deviation was found for the softer site condition, but that deviation was relatively smaller for a proportional change in input motions. Since we did not investigate how much of the nonlinearity and other effects such as the rupture propagation effects had been already included in the GMPEs in Si and Midorikawa (1999) and the residuals analyzed in this study, the equation for correction of nonlinear site amplification should be taken as a general guide rather than the true estimate.

Additional file

Additional file 1. Comparison of the surface and borehole PGVs at the site IBUH03 for the mainshock and a small event.

Abbreviations

3-D: three-dimensional; BA: back-arc; DNL: degree of nonlinearity; FA: fore-arc; F-net: full-range seismograph network; GCMT: global centroid moment tensor; GMPE: ground motion prediction equation; H-to-H: horizontal-to-horizontal; H-to-V: horizontal-to-vertical; JIVSM: Japan integrated velocity structure model; JMA: Japan Meteorological Agency; JST: Japan Standard Time; KiK-net: Kiban Kyoshin network; K-NET: Kyoshin network; Mj: JMA magnitude; Mw: moment magnitude; NEHRP: National Earthquake Hazards Reduction Program; NIED: National Research Institute for Earth Science and Disaster Resilience; P-wave: primary wave; PGA: peak ground acceleration; PGV: peak ground velocity; S-to-B: surface-to-borehole; S-wave: secondary wave/shear wave; USGS: United States Geological Survey; UTC: coordinated universal time; V-to-V: vertical-to-vertical; Vs30: average S-wave velocity in the upper 30 m of the soil layer.

Acknowledgements

We would like to thank the Japan Meteorological Agency for providing us with hypocenter information for the earthquakes used in this study and the strong-motion data. We would also like to thank Wessel and Smith (1998) for providing us with Generic Mapping Tools, which were used to make some figures in the manuscript. We would like to express our sincere thanks to the guest editor Dr. Nobuo Takai and three anonymous reviewers for their constructive comments which helped us to improve the manuscript significantly.

Authors' contributions

YPD analyzed the data and drafted the manuscript. TKs, WS, and SA provided helpful comments. All authors read and approved the manuscript.

Funding

This study was supported by "Advanced Earthquake and Tsunami Forecasting Technologies Project" of NIED.

Availability of data and materials

The strong-motion (K-NET and KiK-net) recordings and PS-loggings used in this study were downloaded from the Web sites: http://www.kyoshin.bosai.go.jp/. The moment magnitude was taken from the Web site: http://www.fnet.bosai.go.jp/event/joho.php?LANG=en. The strong-motion recordings at the JMA sites were retrieved from https://www.data.jma.go.jp/svd/eew/data/ltpgm_explain/data/past/20180906030805/index.html, in Japanese. The hypocenter location and JMA magnitude of the mainshock were taken from the Web site: https://www.data.jma.go.jp/svd/eqev/data/bulletin/hypo_e.html. The hypocenter information of the aftershocks plotted in Fig. 1c, d was taken from https://hinetwww11.bosai.go.jp/auth/JMA/jmalist.php. For other specific information such as the list of recordings used in the study, contact author for data requests.

Competing interests

The authors declare that they have no competing interests.

Received: 21 January 2019 Accepted: 13 May 2019
Published online: 22 May 2019

References

Abrahamson NA, Silva WJ (1997) Empirical response spectral attenuation relations for shallow crustal earthquakes. Seismol Res Lett 68:94–127

Aoi S, Kunugi T, Fujiwara H (2008) Trampoline effect in extreme ground motion. Science 322:728–730. https://doi.org/10.1126/science.1163113

Assimaki D, Li W, Steidl JH, Tsuda K (2008) Site amplification and attenuation via downhole array seismogram inversion: a comparative study of the 2003 Miyagi-oki aftershock sequence. Bull Seismol Soc Am 98:301–330. https://doi.org/10.1785/0120070030

Bonilla LF, Archuleta RJ, Lavallée D (2005) Hysteretic and dilatant behavior of cohesionless soils and their effects on nonlinear site response: field data observations and modeling. Bull Seismol Soc Am 95:2373–2395. https://doi.org/10.1785/0120040128

Boore DM, Joyner WB (1997) Site amplifications for generic rock sites. Bull Seismol Soc Am 87:327–341

Bray JD, Rodriguez-Marek A (2004) Characterization of forward directivity ground motions in the near fault region. Soil Dyn Earthq Eng 24:815–828. https://doi.org/10.1016/j.soildyn.2004.05.001

BSSC (Building Seismic Safety Council) (2003) NEHRP recommended provisions for seismic regulations for new buildings and other Structures (FEMA 450). Report prepared for the Federal Emergency Management Agency (FEMA), National Institute of Building Sciences, Washington, DC

Cabinet Office Japan (2019) About damage situation on the 2018 Hokkaido Eastern Iburi Earthquake (in Japanese), 28 January 2019, 15:00. http://www.bousai.go.jp/updates/h30jishin_hokkaido/pdf/310128_jishin_hokkaido.pdf. Accessed 4 Mar 2019

Campbell KW, Bozorgnia Y (2008) NGA ground motion model for the geometric mean horizontal component of PGA, PGV, PGD and 5% damped linear-elastic response spectra for periods ranging from 0.01 and 10.0 s. Earthq Spectra 24:139–171. https://doi.org/10.1193/1.2857546

Campbell KW, Bozorgnia Y (2014) NGA-West2 ground motion model for the average horizontal components of PGA, PGV, and 5% damped linear acceleration response spectra. Earthq Spectra 30:1087–1115. https://doi.org/10.1193/062913EQS175M

Dhakal YP, Yamanaka H (2012) Delineation of S-wave time window in the Kanto basin for tuning velocity models of deep sedimentary layers. Int Symp Earthq Eng JAEE 1:85–94

Dhakal YP, Takai N, Sasatani T (2010) Empirical analysis of path effects on prediction equations of pseudo-velocity response spectra in northern Japan. Earthq Eng Struct Dyn 39:443–461. https://doi.org/10.1002/eqe.952

Dhakal YP, Aoi S, Kunugi T, Suzuki W, Kimura T (2017) Assessment of nonlinear site response at ocean bottom seismograph sites based on S-wave horizontal-to-vertical spectral ratios: a study at the Sagami Bay area K-NET sites in Japan. Earth Planets Space 69:29. https://doi.org/10.1186/s40623-017-0615-5

Ekström G, Nettles M, Dziewonski AM (2012) The global CMT project 2004–2010: centroid-moment tensors for 13,017 earthquakes. Phys Earth Planet Inter 200–201:1–9. https://doi.org/10.1016/j.pepi.2012.04.002

Fujiwara H, Kawai S, Aoi S, Morikawa N, Senna S, Kudo N, Ooi M, Hao KX, Wakamatsu K, Ishikawa Y, Okumura T, Ishii T, Matsushima S, Hayakawa Y, Toyama N, Narita A (2009) Technical reports on national seismic hazard maps for Japan. Technical note of the National Research Institute for Earth Science and Disaster Prevention: No. 336. http://www.j-shis.bosai.go.jp/en/downloads. Accessed 4 Dec 2018

Garini E, Gazetas G, Anastasopoulos I (2017) Evidence of significant forward rupture directivity aggravated by soil response in an Mw6 earthquake and the effects on monuments. Earthq Eng Struct Dyn 46:2103–2120. https://doi.org/10.1002/eqe.2895

Hardin BO, Drnevich VP (1972) Shear modulus and damping in soils: design equations and curves. J Soil Mech Found Div 98(SM7):667–692

Holzer TL, Youd TL, Hanks TC (1989) Dynamics of liquefaction during the 1987 Superstition Hills, California, earthquake. Science 244:56–59

Iai S, Morita T, Kameoka T, Matsunaga Y, Abiko K (1995) Response of a dense sand deposit during 1993 Kushiro-oki earthquake. Soils Found 35:115–131. https://doi.org/10.3208/sandf1972.35.115

Idriss IM, Seed HB (1968) Seismic response of horizontal soil layers. J Soil Mech Found Div 94(SM4):1003–1031

JMA (Japan Meteorological Agency) (2018a) https://www.jma.go.jp/jma/en/Activities/inttable.pdf. Accessed 27 Nov 2018

JMA (Japan Meteorological Agency) (2018b) http://www.data.jma.go.jp/svd/eqev/data/kyoshin/kaisetsu/calc_sindo.htm, Accessed 27 Nov 2018 (**in Japanese**)

Joyner WB, Boore DM (1981) Peak horizontal acceleration and velocity from strong motion records including records from the 1979 Imperial Valley, California, earthquake. Bull Seismol Soc Am 71:2011–2038

Kaklamanos J, Baise LG, Thompson EM, Dorfmann L (2015) Comparison of 1D linear, equivalent-linear, and nonlinear site response models at six KiK-net validation sites. Soil Dyn Earthq Eng 69:207–219. https://doi.org/10.1016/j.soildyn.2014.10.016

Kamai R, Abrahamson NA, Silva WJ (2014) Nonlinear horizontal site amplification for constraining the NGA-West2 GMPEs. Earthq Spectra 30:1223–1240. https://doi.org/10.1193/070113EQS187M

Kamiyama M (1992) Non-linear soil amplification identified empirically from strong earthquake ground motions. J Phys Earth 40:151–173

Kanno T, Narita A, Morikawa N, Fujiwara H, Fukushima Y (2006) A new attenuation relation for strong ground motion in Japan based on recorded data. Bull Seismol Soc Am 96:879–897. https://doi.org/10.1785/0120050138

Kawase H (1996) The cause of the damage belt in Kobe: the basin-edge effect, constructive interference of the direct S-wave with the basin-induced diffracted/Rayleigh waves. Seismol Res Lett 67(5):25–34

Kawase H, Sanchez-Sesma FJ, Matsushima S (2011) The optimal use of horizontal-to-vertical spectral ratios of earthquake motions for velocity inversions based on diffuse-field theory for plane waves. Bull Seismol Soc Am 101:2001–2014

Kimura G (1996) Collision orogeny at arc-arc junctions in the Japanese Islands. The Island Arc 5:262–275

Kita S, Nakajima J, Hasegawa A, Okada T, Katsumata K, Asano Y, Kimura T (2014) Detailed seismic attenuation structure beneath Hokkaido, northeastern Japan: arc-arc collision process, arc magmatism, and seismotectonics. J Geophys Res Solid Earth 119:6486–6511. https://doi.org/10.1002/2014JB011099

Kitagawa Y, Hiraishi H (2004) Overview of the 1995 Hyogo-Ken Nanbu earthquake and proposals for earthquake mitigation measures. J Jpn Assoc Earthq Eng 4(3):1–29. https://doi.org/10.5610/jaee.4.3_1

Koketsu K, Miyake H, Suzuki H (2012) Japan integrated velocity structure model version 1. In: Proceedings of 15th world conference on earthquake engineering, Lisbon, Portugal, Paper ID 1773

Kramer SL (1996) Geotechnical earthquake engineering. Prentice-Hall Inc, Upper Saddle River, p 653

Midorikawa S, Fukuoka T (1988) Correlation of Japan Meteorological Agency intensity scale with physical parameters of earthquake ground motion. Zisin 41(2):223–233. https://doi.org/10.4294/zisin1948.41.2_223 **(in Japanese with English abstract)**

Midorikawa S, Ohtake Y (2004) Variance of peak ground acceleration and velocity in attenuation relationships. In: Proceedings of the 13th world conference on earthquake engineering, Vancouver, Canada, Paper ID: 325

Midorikawa S, Matsuoka M, and Sakugawa K (1994) Site effects on strong-motion records during the 1987 Chibaken-toho-oki_Japan earthquake. Proceedings of the 9th Japan Earthq Engg Symp Vol 3: 85-90

NEHRP (National Earthquake Hazards Reduction Program) (2019) https://www.nehrp.gov/index.htm. Accessed May 2019

Noguchi S, Sasatani T (2008) Quantification of degree of nonlinear site response. In: Proceedings of the 14th world conference on earthquake engineering, Beijing, China, Paper ID: 03-03-0049

Noguchi S, Sasatani T (2011) Nonlinear soil response and its effects on strong ground motions during the 2003 Miyagi-Oki intraslab earthquake. Zisin 63:165–187. https://doi.org/10.4294/zisin.63.165 **(in Japanese with English abstract)**

Noguchi S, Sato H, Sasatani T (2016) Evaluation of nonlinear soil response during the 2011 off the Pacific coast of Tohoku earthquake by means of simple index of soil nonlinearity. J Jpn Assoc Earthq Eng 16(4):93–105. https://doi.org/10.5610/jaee.16.4_93 **(in Japanese with English abstract)**

Okada Y, Kasahara K, Hori S, Obara K, Sekiguchi S, Fujiwara H, Yamamoto A (2004) Recent progress of seismic observation networks in Japan—Hi-net, F-net, K-NET and KiK-net. Earth Planets Space 56:xv–xxviii. https://doi.org/10.1186/BF03353076

Régnier J, Cadet H, Bonilla LF, Bertrand E, Semblat JF (2013) Assessing nonlinear behavior of soils in seismic site response: statistical analysis on KiK-net strong-motion data. Bull Seismol Soc Am 103:1750–1770. https://doi.org/10.1785/0120120240

Régnier J, Bonilla LF, Bard PV, Bertrand E, Hollender F, Kawase H, Sicilia D, Arduino P, Amorosi A, Asimaki D, Boldini D, Chen L, Chiaradonna A, DeMartin F, Ebrille M, Elgamal A, Falcone G, Foerster E, Foti S, Garini E,

Gazetas G, Gélis C, Ghofrani A, Giannakou A, Gingery JR, Glinsky N, Harmon J, Hashash Y, Iai S, Jeremić B, Kramer S, Kontoe S, Kristek J, Lanzo G, Di Lernia A, Lopez-Caballero F, Marot M, McAllister G, Mercerat ED, Moczo P, Montoya-Noguera S, Musgrove M, Nieto-Ferro A, Pagliaroli A, Pisanò F, Richterova A, Sajana S, Santisi d'Avila MP, Shi J, Silvestri F, Taiebat M, Tropeano G, Verrucci L, Watanabe K (2016) International benchmark on numerical simulations for 1D, nonlinear site response (PRENOLIN): verification phase based on canonical cases. Bull Seismol Soc Am 106:2112–2135. https://doi.org/10.1785/0120150284

Ren Y, Wen R, Yao X, Ji K (2017) Five parameters for the evaluation of the soil nonlinearity during the Ms8.0 Wenchuan earthquake using the HVSR method. Earth Planets Space 69:116. https://doi.org/10.1186/s40623-017-0702-7

Sakai Y (2016) Comparison with the ground motions in the Kumamoto Earthquake (4/16 01:25) and past intensive ground motions. http://www.kz.tsukuba.ac.jp/~sakai/kmm_hk2_en.htm. Accessed 27 Nov 2018

Sato H, Kanatani M (2006) Attenuation characteristics of seismic motion based on earthquake observation records Part2. Proposal of new equivalent linear analysis technique considering attenuation characteristics during strong motion for precise vertical motion simulation. Civil Engineering Research Laboratory Rep. No. N05010 (**in Japanese with English abstract**)

Sato K, Kokusho T, Matsumoto M, Yamada E (1996) Nonlinear seismic response and soil property during strong motion. Soils Found 36:41–52. https://doi.org/10.3208/sandf.36.Special_41

Satoh T, Sato T, Kawase H (1995) Nonlinear behavior of soil sediments identified by using borehole records observed at the Ashigara Valley, Japan. Bull Seismol Soc Am 85:1821–1834

Sawazaki K, Sato H, Nakahara H, Nishimura T (2006) Temporal change in site response caused by earthquake strong motion as revealed from coda spectral ratio measurement. Geophys Res Lett 33:L21303. https://doi.org/10.1029/2006GL027938

Shabestari KT, Yamazaki F (2001) A proposal of instrumental seismic intensity scale compatible with MMI evaluated from three-component acceleration records. Earthq Spectra 17(4):711–723. https://doi.org/10.1193/1.1425814

Si H, Midorikawa S (1999) New attenuation relations for peak ground acceleration and velocity considering effects of fault type and site condition. J Struct Constr Eng Trans AIJ 523:63–70. https://doi.org/10.3130/aijs.64.63_2 **(in Japanese with English abstract)**

Si H, Midorikawa S (2000) New attenuation relations for peak ground acceleration and velocity considering effects of fault type and site condition. In: Proceedings of the 12th world conference on earthquake engineering, Auckland, New Zealand, Paper ID 0532

Steidl JH, Tumarkin AG, Archuleta RJ (1996) What is a reference site? Bull Seismol Soc Am 86:1733–1748

Suzuki W, Aoi S, Kunugi T, Kubo H, Morikawa N, Nakamura H (2017) Strong motions observed by K-NET and KiK-net during the 2016 Kumamoto earthquake sequence. Earth Planets Space 69:19. https://doi.org/10.1186/s40623-017-0604-8

Takahashi H, Kimura R (2019) The 2018 Hokkaido eastern Iburi earthquake and its aftermath. Disaster report: Sc20190112. Journal of Disaster Research 14: Scientific Communication

Tobita T, Iai S, Iwata T (2010) Numerical analysis of near-field asymmetric vertical motion. Bull Seismol Soc Am 100:1456–1469. https://doi.org/10.1785/0120090301

USGS (United States geological Survey) (2018) M 6.6—27 km ENE of Tomakomai, Japan. https://earthquake.usgs.gov/earthquakes/eventpage/us2000h8ty/executive. Accessed on Feb 2019

Walling M, Silva W, Abrahamson N (2008) Nonlinear site amplification factors for constraining the NGA models. Earthq Spectra 24:243–255. https://doi.org/10.1193/1.2934350

Wen KL, Beresnev IA, Yeh YT (1994) Nonlinear soil amplification inferred from downhole strong seismic motion data. Geophys Res Lett 21(24):2625–2628. https://doi.org/10.1029/94GL02407

Wen KL, Chang TM, Lin CM, Chiang HJ (2006a) Identification of nonlinear site response using the H/V spectral ratio method. Terr Atmos Ocean Sci 17(3):533–546

Wen KL, Chang TM, Lin CM, Chiang HJ (2006b) Identification of nonlinear site response during the 1999, Chi–Chi, Taiwan earthquake from the H/V spectral ratio. In: Third international symposium on the effects of surface geology on seismic motion, Grenoble, France, Paper ID 012

Wen KL, Huang JY, Chen CT, Cheng YW (2011) Nonlinear site response of the 2010 Darfield, New Zealand earthquake sequence. In: Fourth international symposium on the effects of surface geology on seismic motion, University of California, Santa Barbara, pp 1–8

Wessel P, Smith WHF (1998) New, improved version of generic mapping tools released. EOS Trans AGU 79:579. https://doi.org/10.1029/98EO00426

Yamada M, Mori J, Heaton T (2009) The slapdown phase in high-acceleration records of large earthquakes. Seismol Res Lett 80:559–564. https://doi.org/10.1785/gssrl.80.4.559

Yamagishi H, Yamazaki F (2018) Landslides by the 2018 Hokkaido Iburi-Tobu earthquake on September 6. Landslides 15:2521–2524. https://doi.org/10.1007/s10346-018-1092-z

Publisher's Note